5.3. Quantitative texture analysis and combined analysis

D. Chateigner, L. Lutterotti and M. Morales

5.3.1. Introduction

For many solids, the growth of single crystals with sufficiently perfect crystallinity is not easy to manage, and is sometimes impossible. On the other hand, a perfectly randomly oriented powder is often impossible to obtain, or may even be undesirable if the anisotropic character of the sample is to be maintained. Consequently, any nondestructive characterization technique (for example diffraction) faces the difficulty of analysing textured samples, which are in a state between a perfect single crystal and a perfect powder. Such 'real samples' are obtained by complex techniques (alignment under uniaxial pressure, magnetic or electric fields, thermal gradients, flux or substrate growth, and combinations of these), and sample preparation is often difficult and time consuming. Unfortunately, when samples are crystallographically oriented to benefit from the intrinsic anisotropic properties of the constituent crystals, many characterization techniques (*i.e.* Rietveld analysis; Rietveld, 1969) are not appropriate or require sample grinding. Very often this grinding is not acceptable, as in the case of rare samples (for example fossils or comets), when grinding modifies the physical properties of the samples themselves (residually stressed materials), or when grinding is simply not possible (thin films).

It then becomes crucial to quantitatively take the textured character of the measured samples into account, either independently of other parameters that are accessible to diffraction (phase content, stresses, particle sizes and shapes), as in quantitative texture analysis (QTA), or to take these parameters into account by refining them all together, as in the combined-analysis (CA) methodology.

In this chapter, we introduce the various aspects of QTA and describe the additional information that CA can yield for the full characterization of real materials. QTA is most commonly applied because the existence of texture often determines the characteristics of the sample.

5.3.2. Crystallographic quantitative texture analysis (QTA)

Even though QTA was developed in the 1960s, the current literature shows that some qualitative information can still be usefully obtained by the simple 'classical' scans used by diffractionists. Such classical scans can be the usual one-dimensional θ–2θ or ω scans (rocking curves) in reflection mode, using point or position-sensitive detectors, or even single images in transmission. We should not forget that such scans can provide (depending on the texture itself) very restricted textural information, which has been thoroughly discussed in Chateigner (2010). There is then *a priori* no justification for using such limited views of texture, particularly with the recent technical advancements in sources and detectors that make the rapid acquisition of full texture scans available.

5.3.2.1. *Orientation distribution (OD)*

5.3.2.1.1. *The orientation space H*

Defining the orientation of a crystal requires the location of at least two directions of the crystal in a macroscopic reference
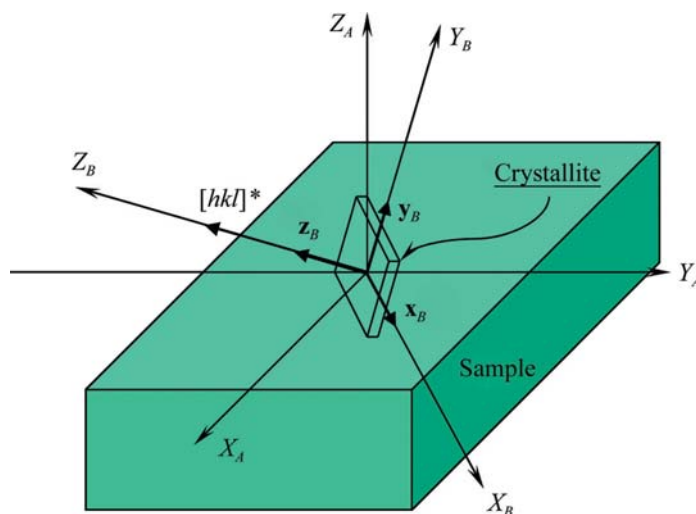

Figure 5.3.1
Crystal and sample reference frames $K_B = (\mathbf{x}_B, \mathbf{y}_B, \mathbf{z}_B)$ and $K_A = (\mathbf{x}_A, \mathbf{y}_A, \mathbf{z}_A)$. Only one crystallite is shown.

frame. The definition of two reference frames (Fig. 5.3.1), one linked to the sample, $K_A = (\mathbf{x}_A, \mathbf{y}_A, \mathbf{z}_A)$, or (**100**, **010**, **001**), and the other to each of the crystals in the sample, K_B, is thus required. In order to make these two frames coincident (Fig. 5.3.2), one needs three Euler angles, α_c, β_c, γ_c, forming a triplet called the orientation component $g = \{\alpha_c, \beta_c, \gamma_c\}$. The angles β_c and α_c determine the orientation of the [001]* crystallite direction in K_A and are called the co-latitude (or pole distance) and azimuth, respectively, while γ_c defines the location of another crystallographic
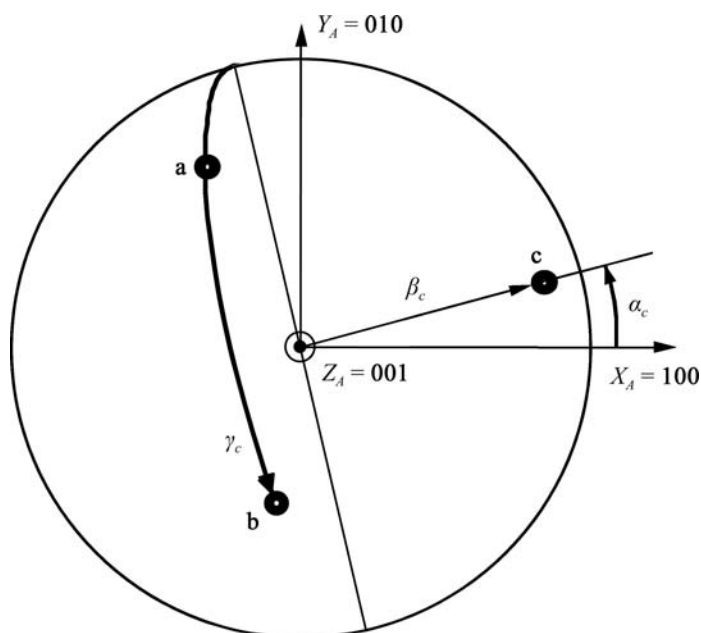

Figure 5.3.2
Definition of the three Euler angles α_c, β_c and γ_c that define the orientation of one crystallite frame $K_B = (\mathbf{a}, \mathbf{b}, \mathbf{c})$ of an orthogonal crystal cell in the sample coordinate system K_A. Note that **100**, **010** and **001** are not Miller indices but are vectors referring to an orthonormal frame aligned with K_A.

direction, chosen as [010]* [in the (**a**, **b**) plane for orthogonal crystal cells].

The ensemble of all possible values of g defines the orientation space, or H space. Note that we use H here (rather than the usual 'G space' for QTA) after the description of orientation symmetry of Curien (1971). An infinite number of possibilities for the choice of Euler angles exist, but the two most commonly used are those of Roe–Matthies (Roe, 1965; Matthies *et al.*, 1987) and Bunge (Bunge, 1969). We use the former here, for which K_A is brought coincident to K_B by the operation $g: [K_A \mapsto K_B]$ using the three following rotations:

(i) rotation of K_A about the axis Z_A through the angle α_c: $[K_A \mapsto K'_A]$; associated rotation $g_1 = \{\alpha_c, 0, 0\}$,

(ii) rotation of K'_A about the axis Y'_A through the angle β_c: $[K'_A \mapsto K''_A]$; associated rotation $g_2 = \{0, \beta_c, 0\}$,

(iii) rotation of K''_A about the axis Z''_A through the angle γ_c: $[K''_A \mapsto K'''_A \parallel K_B]$; associated rotation $g_3 = \{0, 0, \gamma_c\}$.

Finally, we obtain

$$g = g_1 g_2 g_3 = \{\alpha_c, 0, 0\} \{0, \beta_c, 0\} \{0, 0, \gamma_c\} = \{\alpha_c, \beta_c, \gamma_c\}.$$

The choice of K_A has historically been dependent on the field of science. In metallurgy, in dealing with the rolling of metals and alloys (Coulomb, 1982), the normal to the rolling plane (ND), the rolling direction (RD) and its transverse (TD) are typically chosen. For geologists, the sample axes are aligned with respect to the lineation direction and foliation plane, with the track from the latter generally being aligned with the lineation on the pole figures (Wenk, 1985). The use of QTA in molluscan studies (Chateigner *et al.*, 2000) imposed the choice of a frame linked to the mollusc shell growth, margin and normal directions (**G**, **M** and **N**, respectively). In thin-film analyses (Chateigner & Erler, 1997), for which a heteroepitaxial relationship between the film and the underlying single-crystal substrate is generally desired, the sample frame is aligned with the main crystallographic directions of the substrate. In the case of unidirectional experimental environments such as magnetic fields (Morales *et al.*, 2003), fibre spinning, axial pressure (Wenk *et al.*, 1996), hot forging (Guilmeau *et al.*, 2003), spin coating (Ricote & Chateigner, 1999) and self-deposition in a liquid (Manceau *et al.*, 1998), the unique axis (of loading, field or spinning) is generally aligned with the $\mathbf{z_A}$ pole-figure axis. When a combination of several loads is applied, such as a magnetic field and a perpendicular thermal gradient (Durand *et al.*, 1995), the axis of one load is aligned with $\mathbf{z_A}$ while the other is parallel to $\mathbf{x_A}$ or $\mathbf{y_A}$. Using centrifugation, the axis of rotation of the centrifugation is not generally the axis along which the crystal orientation is forced (Gridi-Bennadji *et al.*, 2009), because the pressure axis resulting from centrifugation is radially distributed and is often placed along $\mathbf{z_A}$ in the pole figures, and there is no in-plane alignment in the sample.

5.3.2.1.2. *The orientation distribution (OD) or orientation distribution function (ODF)*

Another concept is needed when dealing with an assembly of many crystals: the orientation distribution of crystallites (or OD), $f(g)$. This function, which can either be represented by an
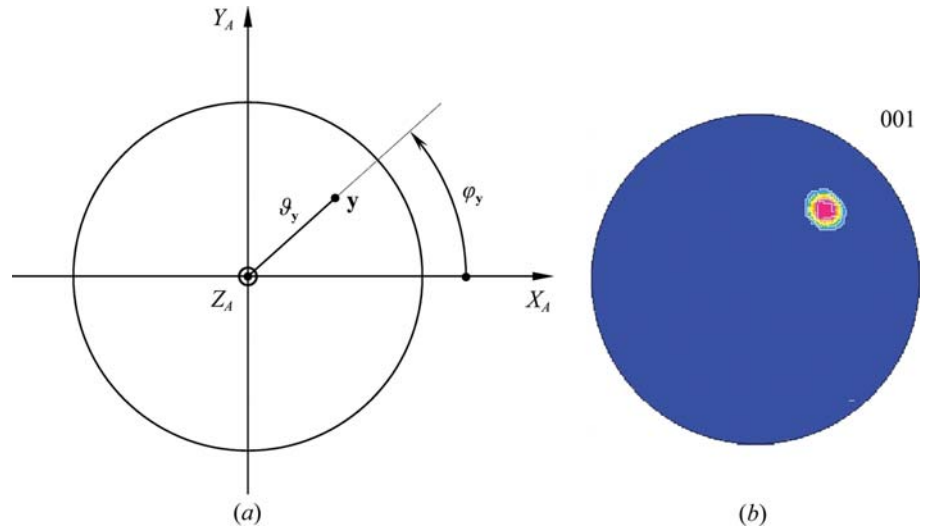

Figure 5.3.3
(*a*) $P_\mathbf{h}(\mathbf{y})$ diffraction pole figure for one crystallite. The direction **y** is associated with the $[hkl]^*$ vector. (*b*) Pole figure of a texture component centred on the previous **y**, with a Gaussian shape with 10° FWHM, for $\mathbf{h} = \langle 001 \rangle^*$ of an orthorhombic crystal structure.

analytical function (ODF) or not (OD), represents the statistical distribution of the orientations of the crystallites in a polycrystalline aggregate. It is defined by

$$\frac{dV(g)}{V} = \frac{1}{8\pi^2} f(g) \, dg, \quad (5.3.1)$$

where $dg = \sin \beta_c \, d\beta_c \, d\alpha_c \, d\gamma_c$ is the orientation element (Fig. 5.3.2) in the orientation space. The H space is constructed from the rotation groups of the crystallographic and sample symmetry (and the inversion centre in normal diffraction). V is the irradiated volume and $dV(g)$ is the volume of crystallites which have an orientation between g and $g + dg$.

$f(g)$ is consequently the volume density of crystallites oriented in dg. It is measured in m.r.d. (multiples of a random distribution) and normalized to the value $f_r(g) = 1$ for a sample without any preferred orientation (random). The $f(g)$ values are orientation distribution densities, and range from 0 (an absence of crystallites oriented in dg around g) to infinity (for some of the H-space values of single crystals). Since V is by definition 100%, the normalization condition of $f(g)$ over the whole orientation space is

$$\int\limits_{\alpha_c=0}^{2\pi} \int\limits_{\beta_c=0}^{\pi} \int\limits_{\gamma_c=0}^{2\pi} f(g) \, dg = 8\pi^2. \quad (5.3.2)$$

5.3.2.1.3. *Pole figures*

5.3.2.1.3.1. *Mathematical expression*

Pole figures, $P_\mathbf{h}(\mathbf{y})$, are representations of the distribution of a given $\mathbf{h} = \langle hkl \rangle^*$ direction in K_A located in Y space (Fig. 5.3.3*a*). They represent the volume density of crystallites oriented in $d\mathbf{y}$, *i.e.* between $(\vartheta_\mathbf{y}, \varphi_\mathbf{y})$ and $(\vartheta_\mathbf{y} + d\vartheta_\mathbf{y}, \varphi_\mathbf{y} + d\varphi_\mathbf{y})$,

$$\frac{dV(\mathbf{y})}{V} = \frac{1}{4\pi} P_\mathbf{h}(\mathbf{y}) \, d\mathbf{y}, \quad (5.3.3)$$

where V is the irradiated volume and $dV(\mathbf{y})$ is the volume of crystallites which have an orientation with a direction $\mathbf{h}$ between $\mathbf{y}$ and $\mathbf{y} + d\mathbf{y}$, with $d\mathbf{y} = \sin \vartheta_\mathbf{y} \, d\vartheta_\mathbf{y} \, d\varphi_\mathbf{y}$. The factor $1/4\pi$ arises from the normalization of the pole figures into distribution densities,

$$\int_{\varphi_{\mathbf{y}}=0}^{2\pi} \int_{\vartheta_{\mathbf{y}}=0}^{\pi} P_{\mathbf{h}}(\vartheta_{\mathbf{y}}, \varphi_{\mathbf{y}}) \sin \vartheta_{\mathbf{y}} \, d\vartheta_{\mathbf{y}} \, d\varphi_{\mathbf{y}} = 4\pi. \qquad (5.3.4)$$

Every pole figure of a random sample will exhibit the same density $P_{\mathbf{h}}(\mathbf{y}) = 1$ m.r.d., whatever the value of $\mathbf{y}$.

5.3.2.1.3.2. Diffraction pole figures and orientation of planes

At a Bragg angle corresponding to the $\{hkl\}$ planes and for a direction $\mathbf{y}$ of the sample, all of the planes such that $\mathbf{h} \| \mathbf{y}$ are in the diffraction condition, whatever their rotation around $\mathbf{y}$. Consequently, diffraction only probes a direction, not an orientation, and we need at least to determine the location of two directions of a plane to know its orientation. Diffraction only probes $P_{\mathbf{h}}(\mathbf{y})$, not $f(g)$ directly, and we need to measure at least several pole figures $P_{\mathbf{h}}(\mathbf{y})$ to determine $f(g)$.

Again, using normal diffraction Friedel's law applies and one cannot differentiate the diffracted intensity $I_{\mathbf{h}}$ from $I_{-\mathbf{h}}$. Consequently, the measured (reduced) pole figures are centrosymmetric and even objects, such that

$$\tilde{P}_{\mathbf{h}}(\mathbf{y}) = \tfrac{1}{2}[P_{\mathbf{h}}(\mathbf{y}) + P_{-\mathbf{h}}(\mathbf{y})]. \qquad (5.3.5)$$

5.3.2.1.3.3. From diffraction measurements to pole figures and ODs

Diffraction pole figures are usually measured using a four-circle diffractometer with regular increments in tilt (χ) and azimuth (φ) rotation axes, or in kappa geometry. Both reflection (Schulz, 1949a) and transmission (Schulz, 1949b; Field & Merchant, 1949) modes can be used, with point, one-dimensional or two-dimensional detectors, which can be either linear, flat or curved.

Prior to any measurement, it is necessary to know whether the data available from a given instrument can provide a correct OD characterization (*i.e.* how many pole figures are necessary and over which range each pole figure has to be measured) in order to permit an OD refinement. Helming (1992) addressed the question with the minimum pole-figure range, using the minimum pole density set concept of Vadon (1981). Such an approach defines as a necessary condition that the number and range of pole figures must be large enough such that any crystal orientation can be determined unambiguously. Using discrete data points, this requires that at least three projection paths $\tilde{\varphi}$ from pole figures pass through every OD cell. Complete OD coverage requires quite a large amount of data (typically 1300 measured points per pole figure, with several pole figures being necessary for low resolution using a 5° grid), which is nowadays accessible using multiple detectors.

The goniometer setting for each point can be described by three angles: ω, χ and φ. Additionally, if the diffraction point that we consider (the detector or pixel position) is outside the usual 2θ diffraction plane, another angle η is necessary along the Debye ring. We can define the resulting rotation matrix $\mathbf{R}$ as the product of the corresponding 3×3 matrices,

$$\mathbf{R} = -\mathbf{\Theta H \Omega X \Phi}, \qquad (5.3.6)$$

and the pole-figure angles can be obtained:

$$\cos \vartheta_{\mathbf{y}} = R_{33},$$
$$\tan \varphi_{\mathbf{y}} = R_{31}/R_{32}. \qquad (5.3.7)$$

Depending on the experimental setup, various corrections have to be applied to the data. Localization corrections are those that transform the angular coordinates of the data from the diffractometer space S, where the scattered intensities are measured, to the space in which modelling occurs, for instance the pole-figure space Y (Bunge *et al.*, 1982; Heizmann & Laruelle, 1986; Heidelbach *et al.*, 1999; Chateigner, 2010). Also, depending on the sample itself, proper corrections for defocusing and background (Chernock & Beck, 1952; Gale & Griffiths, 1960; Holland, 1964; Feng, 1965; Tenckhoff, 1970; Couterne & Cizeron, 1971; Huijser-Gerits & Rieck, 1974), fluorescence, absorption and volume changes (Chateigner *et al.*, 1992, 1994a,b, 1995; Liu *et al.*, 2003) have to be carried out during sample rotations. The representation of pole figures is usually by stereographic (or equal-angular) projections. The main drawback of such a representation is that the density levels at the centre of the pole figures appear to be overrepresented compared with those near the equator. We then prefer to plot pole figures using Schmidt (or Lambert) projections (or equal-area projections), which offer representations with nearly equal surface elements at the centres and peripheries of pole figures (Kocks *et al.*, 1998).

After the previous corrections, one obtains the so-called diffraction (direct) pole figures, $I_{\mathbf{h}}(\mathbf{y})$. However, these depend on the porosity, crystalline state and other features of the sample, and to compare textures between samples the normalized pole figure $P_{\mathbf{h}}(\mathbf{y})$ has to be calculated.

Such normalization, calculations and refinements of the ODs using various algorithms are implemented in software such as the *Berkeley Texture* (*BEARTEX*) package (Wenk *et al.*, 1998), the *Preferred Orientation Package – Los Alamos* (*popLA*) package (Kocks *et al.*, 1994), the *LaboTex* texture-analysis software (Pawlik & Ozga, 1999) and the *MATLAB* toolbox for quantitative texture analysis (*MTEX*; Hielscher & Schaeben, 2008). The last is freeware. Two other programs, *Material Analysis Using Diffraction* (*MAUD*; Lutterotti *et al.*, 1999) and the *General Structure Analysis System* (*GSAS*; Von Dreele, 1997; Larson & Von Dreele, 2000), are furthermore able to carry out Rietveld analysis on large sets of data, giving access to many more material characteristics.

5.3.2.1.3.4. Pole-figure normalization

If a given $I_{\mathbf{h}}(\mathbf{y})$ pole figure has been measured completely (all of the $\mathbf{y}$ values could be obtained), it can be normalized
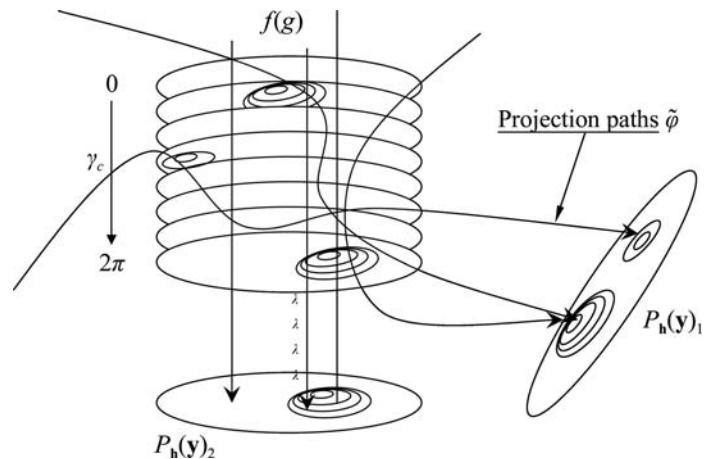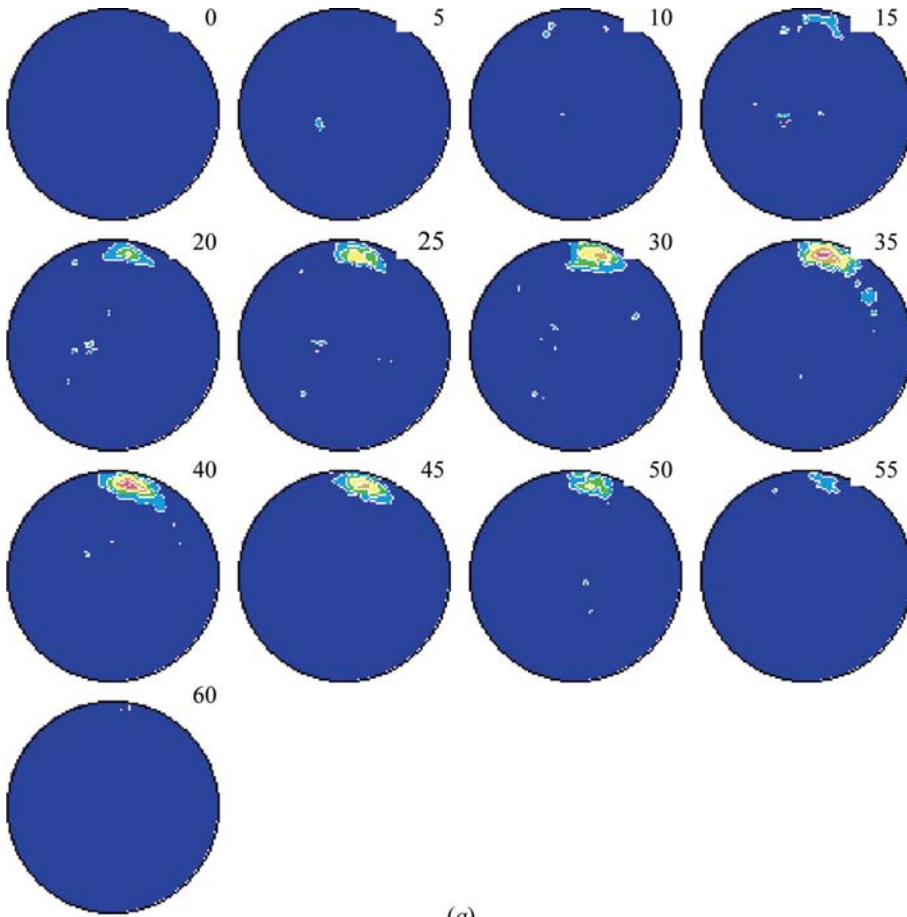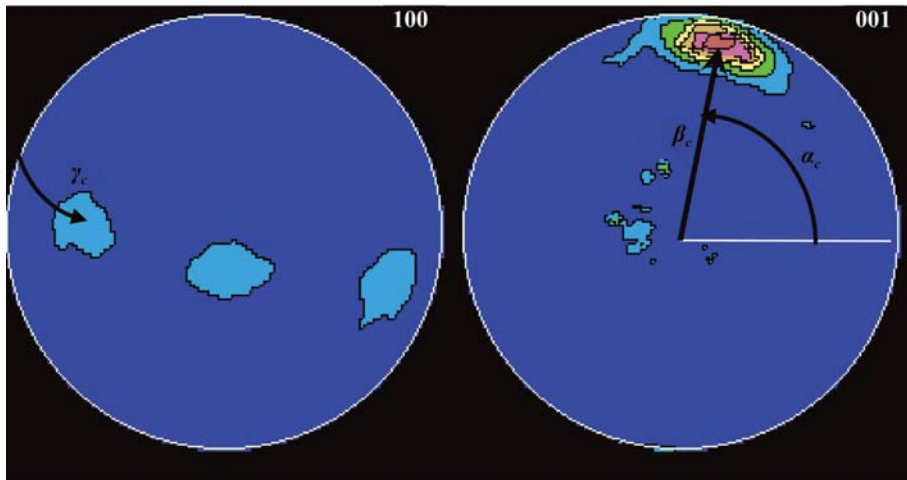

Figure 5.3.4
Relationship between the three-dimensional object $f(g)$ and the pole figures $P_{\mathbf{h}}(\mathbf{y})$. Several OD boxes correspond to each pole figure cell, and each OD box is linked to several pole-figure cells.

(a)

(b)

Figure 5.3.5
(a) An OD as γ_c sections and (b) as {100} and {001} pole figures.

$$N_{\mathbf{h}} = I_{\mathbf{h}}^t \bigg/ \int\limits_{\varphi_{\mathbf{y}}=0}^{2\pi} \int\limits_{\vartheta_{\mathbf{y}}=0}^{\pi/2} \sin\vartheta_{\mathbf{y}}\, d\vartheta_{\mathbf{y}}\, d\varphi_{\mathbf{y}}, \quad (5.3.9)$$

which is necessary for calculation of the normalized pole figure (expressed in m.r.d. units),

$$P_{\mathbf{h}}(\mathbf{y}) = \frac{I_{\mathbf{h}}(\mathbf{y})}{N_{\mathbf{h}}}. \quad (5.3.10)$$

However, experimental considerations mean that the pole figures are generally not measured completely, and the $N_{\mathbf{h}}$ factors are usually refined during the OD calculation (see Section 5.3.2.3.1).

5.3.2.2. *The fundamental equation of quantitative texture analysis*

Since a pole figure measures the distribution of only one direction type $\langle hkl\rangle^*$, it does not probe an orientation directly. Phrased differently, any rotation around this specific vector by an angle $\tilde{\varphi}$ results in the same diffracted intensity. From (5.3.1) and (5.3.3), one can obtain the fundamental equation of QTA,

$$P_{\mathbf{h}}(\mathbf{y}) = \frac{1}{2\pi} \int\limits_{\mathbf{h}\|\mathbf{y}} f(g)\, d\tilde{\varphi}, \quad (5.3.11)$$

which represents the fact that each pole figure (which is a two-dimensional object) is a projection along a certain path $\tilde{\varphi}$ of the OD (a three-dimensional object) which depends on the crystal symmetry (Fig. 5.3.4). Each cell of a given pole figure will then be an average over several cells of the OD, and each cell of the OD will be measured by one or more cells from the pole figures. The larger the number of pole-figure cells that measure a specific OD cell, the more statistically reliable the measurement of this OD is. In practice, one has to measure the largest number possible of reliable (sufficiently intense) pole figures to define the OD with the best resolution available.

For instance, an OD of a hexagonal system represented by a series of γ_c sections (Fig. 5.3.5a) may reveal a maximum pole density for a γ_c value of 35°. The corresponding {100} and {001} pole figures (Fig. 5.3.5b) illustrate the meaning of γ_c in the pole-figure space for this single-component texture. In the {001} pole figure, the pole maximum is located at $(\varphi_{\mathbf{y}}, \vartheta_{\mathbf{y}}) = (\alpha_c, \beta_c) = (85°, 80°)$. Since γ_c locates the **b** axis, with this latter being represented by the {100} pole figure, $\gamma_c = 35°$ is the angle between the equator and **b** in this pole figure. Users should not be afraid to build a three-dimensional model of the unit-cell axes to assist in interpreting such pole figures.

Let us mention at this point that the pole figures that are obtained using normal diffraction methods are so-called reduced pole figures, $\tilde{P}_{\mathbf{h}}(\mathbf{y})$. Friedel's law requires that the measured pole figures are superpositions of $+\mathbf{h}$ and $-\mathbf{h}$ true pole figures. This fact (which is even the case for anomalous

directly. Since whatever the texture state of a given sample is (*i.e.* whether the sample exhibits a texture or is randomly oriented) the total intensity scattered by the sample $I_{\mathbf{h}}^t$ must be the same, the sum of all intensities $I_{\mathbf{h}}(\mathbf{y})$ collected on the hemisphere is the same, all other sample characteristics being constant:

$$I_{\mathbf{h}}^t = \int\limits_{\varphi_{\mathbf{y}}=0}^{2\pi} \int\limits_{\vartheta_{\mathbf{y}}=0}^{\pi/2} I_{\mathbf{h}}(\vartheta_{\mathbf{y}}, \varphi_{\mathbf{y}}) \sin\vartheta_{\mathbf{y}}\, d\vartheta_{\mathbf{y}}\, d\varphi_{\mathbf{y}}. \quad (5.3.8)$$

One can then obtain the intensity $N_{\mathbf{h}}$ that would diffract from this sample for the **h** pole figure if it was randomly oriented,

scattering in the case of centrosymmetric crystals) leads to the presence of 'ghost' phenomena (Matthies & Vinel, 1982; Matthies *et al.*, 1987). The true, unreduced or 'complete' pole figure is defined as

$$P_{\mathbf{h}}(\mathbf{y}) = \tilde{P}_{\mathbf{h}}(\mathbf{y}) + \tilde{\tilde{P}}_{\mathbf{h}}(\mathbf{y}), \qquad (5.3.12)$$

in which $\tilde{\tilde{P}}_{\mathbf{h}}(\mathbf{y})$ is the nonmeasured part of the pole figures. We will not take account of this here since ghost suppression, if possible, would require anomalous diffraction and very intense beams. Instead, theoretically derived ghost-correcting approximations can be used. However, it should be strongly emphasized here that in the case of noncentrosymmetric crystal symmetry the ODF will not be determined completely.

5.3.2.3. *Resolution of the fundamental equation*

5.3.2.3.1. *Generalized spherical-harmonics expansion*

The solution proposed by Bunge & Esling (1982) consists of describing the OD and the pole figures as series of generalized spherical harmonics,

$$f(g) = \sum_{\lambda=0}^{\infty} \sum_{m=-\lambda}^{\lambda} \sum_{n=\lambda}^{\lambda} C_{\lambda}^{mn} T_{\lambda}^{mn}(g), \qquad (5.3.13)$$

$$P_{\mathbf{h}}(\mathbf{y}) = \sum_{\lambda=0}^{\infty} \frac{4\pi}{2\lambda+1} \sum_{n=-\lambda}^{\lambda} k_{\lambda}^{n}(\mathbf{y}) \sum_{m=-\lambda}^{\lambda} C_{\lambda}^{mn} k_{\lambda}^{*m}(\Theta_{\mathbf{h}}\phi_{\mathbf{h}}). \qquad (5.3.14)$$

(5.3.11) still holds, and in this approach one has to determine the C_{λ}^{mn} coefficients, which are the proportions of the respective $T_{\lambda}^{mn}(g)$ and depend on the texture, from the experiments. The $T_{\lambda}^{mn}(g)$ are known generalized spherical harmonics which depend on the crystal and texture symmetries. The series expands on both even and odd values of λ. In practice, the expansion on λ cannot be infinite and is limited to a value L, the maximum degree of series expansion, which fixes the angular resolution of the expansion. k_{λ}^{n} and k_{λ}^{*m} are spherical harmonics based on Legendre polynomials (Bunge & Esling, 1982). The angles $\Theta_{\mathbf{h}}$ and $\phi_{\mathbf{h}}$ are the spherical coordinates of the $\mathbf{h}$ direction in the crystal reference frame. The number of C_{λ}^{mn} coefficients and the extension L to which the series in (5.3.14) has to be expanded in λ are also dependent on the crystal and texture symmetries.

If a certain number of pole-figure values are measured for different crystallographic directions $\mathbf{h}$, then a set of linear equations can be set up using (5.3.14) and solved. There are three commonly used methods to obtain the C_{λ}^{mn} coefficients.

The first method can be used only if complete pole figures are measured, in which case (5.3.14) can be written

$$P_{\mathbf{h}}(\mathbf{y}) = \sum_{\lambda=0}^{\infty} \sum_{n=-\lambda}^{\lambda} F_{\lambda}^{n}(\mathbf{h}) k_{\lambda}^{n}(\mathbf{y}) \qquad (5.3.14a)$$

and

$$F_{\lambda}^{n}(\mathbf{h}) = \frac{4\pi}{2\lambda+1} \sum_{m=-\lambda=0}^{\lambda} C_{\lambda}^{mn} k_{\lambda}^{*m}(\Theta_{\mathbf{h}}, \phi_{\mathbf{h}}) \sum_{n=-\lambda}^{\lambda} F_{\lambda}^{n}(\mathbf{h}) k_{\lambda}^{n}(\mathbf{y}). \qquad (5.3.14b)$$

Multiplying both sides of (5.3.14a) by $k_{\lambda}^{*m}(\mathbf{y})$ and integrating over the whole sphere then yields

$$F_{\lambda}^{n}(\mathbf{h}) = \int P_{\mathbf{h}}(\mathbf{y}) k_{\lambda}^{*n}(\mathbf{y}) \, \mathrm{d}\mathbf{y}$$
$$= \int_{\vartheta_{\mathbf{y}}}^{\pi} \int_{\varphi_{\mathbf{y}}}^{2\pi} P_{\mathbf{h}}(\vartheta_{\mathbf{y}}, \varphi_{\mathbf{y}}) k_{\lambda}^{*n}(\vartheta_{\mathbf{y}}, \varphi_{\mathbf{y}}) \sin \theta_{\mathbf{y}} \, \mathrm{d}\vartheta_{\mathbf{y}} \, \mathrm{d}\varphi_{\mathbf{y}}. \qquad (5.3.14c)$$

The first step of the procedure is to compute the quantities $F_{\lambda}^{n}(\mathbf{h})$ from (5.3.14c) using the measured pole-figure values. In the second step (transformation of coefficients), the system of linear equations (5.3.14b) solved for the variables C_{λ}^{mn} and $f(g)$ is determined.

The second method is used when it is not possible to measure complete pole figures and consequently the quantities in (5.3.14c) cannot be computed. In such a case, we refer the reader to Chapter 7 of Bunge & Esling (1982) for a complete exposition. The method also solves a system of linear equations to obtain the harmonic coefficients:

$$\sum_{\lambda=0}^{L} \sum_{m=1}^{M(\lambda)} \sum_{n=1}^{N(\lambda)} C_{\lambda}^{mn} \left[\alpha_{\lambda\lambda'}^{mm'} \zeta_{\lambda\lambda'}^{nn'} - \sum_{\mathbf{h}} \frac{a_{\lambda}^{mn}(\mathbf{h}) a_{\lambda'}^{m'n'}(\mathbf{h})}{P_{\mathbf{h}}} \right] = 0 \qquad (5.3.14d)$$

and

$$P_{\mathbf{h}} = 2 \int_{B} [I_{\mathbf{h}}(\mathbf{y})]^2 \, \mathrm{d}\mathbf{y},$$

where B is the measured range in the pole figure,

$$a_{\lambda}^{mn}(\mathbf{h}) = 2 \frac{4\pi}{2\lambda+1} \dot{k}_{\lambda}^{*m}(\Theta_{\mathbf{h}}, \phi_{\mathbf{h}}) \int_{B} I_{\mathbf{h}}(\mathbf{y}) \dot{k}_{\lambda}^{n}(\mathbf{y}) \, \mathrm{d}\mathbf{y},$$

$$\zeta_{\lambda\lambda'}^{nn'} = 2 \int_{B} \dot{k}_{\lambda'}^{n'}(\mathbf{y}) \dot{k}_{\lambda}^{n}(\mathbf{y}) \, \mathrm{d}\mathbf{y},$$

$$a_{\lambda\lambda'}^{mm'} = \frac{4\pi}{2\lambda+1} \frac{4\pi}{2\lambda'+1} \sum_{\mathbf{h}} \dot{k}_{\lambda}^{*m}(\Theta_{\mathbf{h}}, \phi_{\mathbf{h}}) \dot{k}_{\lambda'}^{*m'}(\Theta_{\mathbf{h}}, \phi_{\mathbf{h}}).$$

The third method uses the minimization procedure of (5.3.15) to refine the harmonic coefficients by a least-squares method, through which the $P_{\mathbf{h}}(\mathbf{y})$ are expressed using (5.3.14):

$$\sum_{\mathbf{h}} \oint [I_{\mathbf{h}}(\mathbf{y}) - N_{\mathbf{h}} P_{\mathbf{h}}(\mathbf{y})]^2 \, \mathrm{d}\mathbf{y} = \min. \qquad (5.3.15)$$

The integral is substituted by a summation over the entire measured range of the pole figures (complete or incomplete).

For strongly textured samples, the harmonics formulation creates strong negative density values, in particular if the expansion is restricted to too low an L value (which unfortunately can be the case experimentally if insufficient pole figures can be measured), and has been proved to be less adequate than other discrete methods. Several methods have been developed to correct for this artifact, all of which force negative densities to zero (Wenk *et al.*, 1988). However, forcing densities to zero wherever they appear to be negative (if physically more reasonable) may appear to be a little arbitrary. This feeling may be reinforced by the fact that ghosts can also be positive, with these latter not being subject to the same 'correction' possibilities. However, one advantage of using a harmonic series is that it provides the necessary material for the simplest approximation of the mechanical property simulations with a limited number of coefficients to be refined (the C_{λ}^{mn} values). These coefficients can also be computed from the OD obtained by other methods.

Since $f(g)$ is a density, one should observe $f(g) \geq 0$ for all g values, or 'positivity'. From (5.3.5) we know that the measured or reduced pole figures are centrosymmetric, and as a consequence of (5.3.14) only the even-order coefficients can be determined by diffraction. On the other hand there are even and odd coefficients in $f(g)$, and two different ODs have then to be considered, depending on the parity of the λ terms,

$$f(g) = f^e(g) + f^o(g), \qquad (5.3.16)$$

and here $f(g)$ and $f^o(g)$ are two unknowns, with the even part of the harmonic series $f^e(g)$ being the part that is accessible to normal diffraction; the odd part is measurable in certain cases using anomalous scattering. This phenomenon creates ghosts (negative, unphysical distribution densities) in the OD (Matthies, 1979; Matthies & Vinel, 1982), which are undesirable for a quantitative description of $f(g)$. An approximate 'ghost correction' by estimating the odd coefficients is more or less complicated in the harmonic formalism (Esling *et al.*, 1982). Some approaches for this correction have been developed such as the 'positivity method' (Dahms & Bunge, 1988; Wagner & Dahms, 1991) or the 'GHOST' and 'quadratic' methods (Van Houtte, 1983, 1991), all of which still permit some residual negative densities (see Section 5.3.2.3.8).

5.3.2.3.2. *Vector method*

This discrete method (Ruer, 1976; Ruer & Baro, 1977; Vadon, 1981) works in direct space. Here, $f(g)$ is represented by a vector called the 'texture vector' $\mathbf{f}_j$, $j = 1, \ldots, J$, with J the number of cells in which $f(g)$ is discretized. This number, of course, depends on the resolution of the measurement scans of the pole figures. Each pole figure is represented by $\mathbf{P}_i(\mathbf{h})$, $i = 1, \ldots, N$, with N being the number of cells of the pole figure. The fundamental equation of QTA becomes

$$P_i(\mathbf{h}) = [\boldsymbol{\sigma}_{ij}(\mathbf{h})]\mathbf{f}_j, \qquad (5.3.17)$$

in which $\boldsymbol{\sigma}_{ij}(\mathbf{h})$ is a rectangular matrix. The fundamental problem therefore consists of finding the solution to the system of linear equations (5.3.17).

5.3.2.3.3. *WIMV method*

The WIMV approach [where WIMV is an acronym from Williams (1968), Imhof (1982) and Matthies & Vinel (1982)] is an iterative method which ensures a conditional ghost correction. It is based on the numerical refinement of $f(g)$ at step $n + 1$,

$$f^{n+1}(g) = \hat{N} \frac{f^n(g)f^0(g)}{\prod_{i=1}^{I}\left[\prod_{m=1}^{M_{\mathbf{h}i}} P_{\mathbf{h}_{im}}^n(\mathbf{y})\right]^{1/IM_{\mathbf{h}i}}}, \qquad (5.3.18)$$

where the product extends over the I experimentally measured pole figures and the multiplicity is $M_{\mathbf{h}}$ for all the poles. $f^n(g)$ and $P_{\mathbf{h}}^n(\mathbf{y})$ represent the refined values of $f(g)$ and $P_{\mathbf{h}}(\mathbf{y})$ at the nth step, respectively. $\hat{N}$ is the normalization operation. The $P_{\mathbf{h}_{im}}^n(\mathbf{y})$ values are calculated at each cycle with (5.3.12). The first step in this procedure is to evaluate $f^0(g)$,

$$f^0(g) = \hat{N}\prod_{i=1}^{I}\left[\prod_{m=1}^{M_{\mathbf{h}i}} P_{\mathbf{h}_{im}}^{\exp}(\mathbf{y})\right]^{1/IM_{\mathbf{h}i}}, \qquad (5.3.19)$$

in which $P_{\mathbf{h}}^{\exp}(\mathbf{y})$ represents the measured pole figures. The WIMV algorithm maximizes the so-called 'phon' (orientation background or minimum value of the OD which represents the randomly oriented fraction of the sample) and the texture sharpness. While in the previous methods of OD resolution low texture and crystal symmetries give rise to large amounts of data to store and long computation times, the WIMV approach does not depend greatly on these symmetries. Other methods have been derived from WIMV and they maintain the same iteration structure as depicted in (5.3.18); they are described in Sections 5.3.2.3.4, 5.3.2.3.5 and 5.3.2.3.6.

5.3.2.3.4. *Arbitrarily defined cells (ADC) method*

Essentially based on a WIMV-like algorithm (Pawlik, 1993), the ADC method uses projection tubes instead of projection paths. Each cell volume is then taken into account in the calculations, which gives a better smoothing scheme. A similar concept is also used in the EWIMV approach and is described in Section 5.3.2.3.6.

5.3.2.3.5. *Entropy-maximization method*

This method (Schaeben, 1988, 1991*a*,*b*) is based on the maximization of the texture 'disorder' or texture entropy, *i.e.* trying to obtain the maximum texture phon from a set of experiments. Following information theory (Shannon, 1948), the entropy estimator in texture can be described by

$$S = -\sum_{i} f(g_i) \ln f(g_i), \qquad (5.3.20)$$

which results in the iterative procedure

$$f^{n+1}(g) = f^n(g)\prod_{i=1}^{I}\prod_{m=1}^{M_{\mathbf{h}i}}\left[\frac{P_{\mathbf{h}}(\mathbf{y})}{P_{\mathbf{h}}^n(\mathbf{y})}\right]^{r_n/IM_{\mathbf{h}i}}, \qquad (5.3.21)$$

in which r_n is a relaxation parameter such that $0 < r_n < 1$.

5.3.2.3.6. *EWIMV method*

When the WIMV calculation is inserted into the Rietveld refinement procedure, it requires two additional steps:
 (i) the extraction of the pole-figure or texture weights,
(ii) the interpolation of these weights to fit a regular grid (imposed by the original WIMV algorithm).
The latter yields non-optimized values of the OD, particularly for sharp textures and coarse irregular coverage of the OD. The entropy-modified WIMV (EWIMV) method has proved to be effective as an extension of the WIMV method (Lutterotti *et al.*, 2004; Morales *et al.*, 2002). In this latter the OD cell values are computed through an entropy iteration algorithm as in (5.3.21), with incorporation of the reflection weights $w_{\mathbf{h}}$:

$$f^{n+1}(g) = \hat{N}f^n(g)\prod_{h=1}^{I}\prod_{m=1}^{M_{\mathbf{h}i}}\left[\frac{P_{\mathbf{h}_{im}}(\mathbf{y})}{P_{\mathbf{h}_{im}}^n(\mathbf{y})}\right]^{r_n w_{\mathbf{h}}/IM_{\mathbf{h}i}}. \qquad (5.3.22)$$

$w_{\mathbf{h}}$ is introduced to take into account the different accuracy of the more intense and less overlapped reflections with respect to the smaller reflections, and is calculated analogously to the weight factors in the Rietveld analysis. In (5.3.22), the integration path is computed using a similar concept to the tube projection introduced by the ADC method (Section 5.3.2.3.4). In the case of EWIMV the projection for each integration point is calculated using all of the neighbouring cells in the OD to that in which the integration point falls, and the cell contribution is weighted using the reciprocal of the distance between the centre of the cell and the exact integration-point position. This has also a positive effect on smoothing out the noise from the OD and increases the experimental 'coverage' of the OD.

5.3.2.3.7. *Component method*

For very strong textures most of the orientation space cells have zero values, while a few cells exhibit very large distribution densities. In such cases the number of data to be acquired can be tremendously large and tends to an unacceptable limit. However, since the OD is described by a small number of orientations g, simple functions can be used to represent it, and the g values are

easily handled. Let a specific texture component (Helming, 1992) centred at the orientation $g = g^c$ be represented by the model function $f^c(g)$. The total OD can be represented by

$$f(g) = F + \sum_c I^c f^c(g), \qquad (5.3.23)$$

where the intensity I^c is the volume fraction of crystallites belonging to the component g^c of distribution $f^c(g)$, and F represents the volume fraction of randomly oriented crystallites. For consistency, the components have to respect the normalization conditions

$$F + \sum_c I^c = 1 \text{ and } \sum_c f^c(g) = 1. \qquad (5.3.24)$$

The $f^c(g)$ components can be represented by any function, *i.e.* Gaussian, Lorentzian or elliptical distributions (Matthies *et al.*, 1987), that is normalized. Generally, two types of components are used: spherical (Matthies, 1980, 1982) and fibre (Matthies *et al.*, 1988). Each component may then have a Gaussian or Lorentzian character.

Spherical components are described by an orientation position g_0 in the OD space and a half-width at half-maximum, b, to characterize the shape of the distribution ($0 \leq b \leq 2\pi$). Taking $\tilde{\omega}$ as the angular distance between an orientation g and g_0, the Gaussian spherical component can be written as

$$f(g_0, b, g) = f(S, \tilde{\omega}) = N(S) \exp(S \cos \tilde{\omega}), \qquad (5.3.24a)$$

with $0 \leq \tilde{\omega} = \tilde{\omega}(g_0, g) \leq \pi$, $0 \leq S \leq \infty$, $S = \ln 2 / [2 \sin^2(b/4)]$;

$$N(S) = [I_0(S) - I_1(S)]^{-1} \qquad (5.3.24b)$$

is the normalization factor and $I_n(x)$ are the modified Bessel functions:

$$I_n(x) = \frac{1}{\pi} \int_0^\pi \exp[x \cos(t)] \cos(nt) \, \mathrm{d}t. \qquad (5.3.24c)$$

Now the unreduced pole-figure value by integration using (5.3.9) becomes

$$P_\mathbf{h}(g_0, b, \mathbf{y}) = P(S, z) = N(S) I_0 \left[\frac{S(z+1)}{2} \right] \exp \left[\frac{S(z-1)}{2} \right], \qquad (5.3.25)$$

with $z = \mathbf{h} \cdot g_0 \cdot \mathbf{y}$.

Since the reduced pole figure is the measured one (Section 5.3.2.3.1), it must be computed as (using equation 5.3.5),

$$\bar{P}(S, z) = \frac{P(S, z) - P(S, -z)}{2}. \qquad (5.3.26)$$

Similarly, for a Lorentzian spherical component

$$f(g_0, b, g) = f(t, \tilde{\omega}) = (1 - t^2) \frac{(1 + t^2)^2 + 4t^2 \cos^2(\tilde{\omega}/2)}{[(1 + t^2)^2 - 4t^2 \cos^2(\tilde{\omega}/2)]^2}, \qquad (5.3.27)$$

where

$$t = \tau^{1/2} - (\tau - 1)^{1/2},$$
$$c = \cos^2(b/4),$$
$$w = (19c^2 - 34c + 19)^{1/2},$$
$$\tau = \frac{2w}{3} \cos \left[\frac{1}{3} \cos^{-1} \left(\frac{-82c^3 + 240c^2 - 246c + 80}{w^3} \right) \right] + \frac{5 - 4c}{3},$$

and the unreduced pole-figure value becomes

$$P_\mathbf{h}(g_0, b, y) = P(t, z) = \frac{1 - t^4}{(1 - 2t^2 z + t^4)^{3/2}}. \qquad (5.3.28)$$

A Gaussian-like fibre component is defined by two vectors $(\mathbf{h}_0, \mathbf{n}_0)$ and the half-width b. $\mathbf{n}_0$ is the fibre direction in the sample coordinates and $\mathbf{h}_0$ is the fibre direction in the crystal coordinate system. Then,

$$f(\mathbf{h}_0, \mathbf{n}_0, b, g) = f(S, z) = \left[\frac{S}{\sinh(S)} \right] \exp(Sz), \qquad (5.3.29)$$

in which z and S have been already defined for the Gaussian component. The unreduced pole figures can now be computed as

$$P(S, z_1, z_2) = \frac{S}{\sinh(S)} I_0 \left[S(1 - z_1^2)^{1/2}(1 - z_2^2)^{1/2} \right] \exp(Sz_1 z_2), \qquad (5.3.30)$$

where

$$z_1 = \mathbf{h} \cdot \mathbf{h}_0, \quad z_2 = \mathbf{y} \cdot \mathbf{n}_0.$$

In the case of a Lorentzian fibre component, using the same definitions as for the Gaussian fibre component the equations are

$$f(\mathbf{h}_0, \mathbf{n}_0, b, g) = f(t_f, z) = \frac{1 - t_f}{(1 - 2t_f z + t_f^2)^{3/2}}, \qquad (5.3.31)$$

where

$$t_f = R - (R^2 - 1)^{1/2},$$
$$R = \frac{2^{2/3} - \cos(b/4)}{2^{2/3} - 1}$$

and the reduced pole figure is

$$P(t_f, z_1, z_2) = \frac{2}{\pi} \frac{1 - t_f^2}{(C - D)(C + D)^{1/2}} E \left(\frac{2D}{C + D} \right),$$
$$C = 1 + t_f^2 - 2t_f z_1 z_2,$$
$$D = 2t_f (1 - z_1^2)^{1/2}(1 - z_2^2)^{1/2}$$

and $E(k)$ is the complete elliptic integral of the second kind,

$$E(k) = \int_0^{\pi/2} (1 - k^2 \sin^2 \theta)^{1/2} \, \mathrm{d}\theta.$$

5.3.2.3.8. *Positivity and exponential harmonics*

In the positivity and exponential method the idea is to use and determine the odd coefficients that may ensure a positive $f(g)$. In the positivity method the even coefficients are not modified (as they are linked to the experimental pole figures) and the odd coefficients do not affect the computation. For a detailed description of the positivity algorithm, we refer to the original articles (Dahms & Bunge, 1988; Van Houtte, 1991). The goal of the algorithm is to determine the odd coefficients corresponding to an OD equal to (with sign inverted) the negative part of the OD found from the experimental data, $f_0(g)$,

$$C_\lambda^{mn} = -(2\lambda + 1) \int_{\forall g \in Z-} f_0(g) T_\lambda^{mn}(g) \, \mathrm{d}g, \qquad (5.3.32)$$

where $Z-$ is the orientation space over which the $f_0(g)$ values are negative or lower than a given threshold α defining the OD background. Moreover, it has been recognized that most of the time there are a set of odd coefficients that are able to completely eliminate all negative parts of the OD, maintaining the even coefficients constant. Another way to ensure OD positivity (Van

Houtte, 1991) is to express it with functions that result in values that are always positive, such as exponentials with real function arguments $h(g)$. For instance, using $f(g) = \exp[h(g)] \geq 0$, (5.3.13) and (5.3.14) become

$$\exp[h(g)] = \sum_{\lambda=0}^{L} \sum_{m=1}^{M(\lambda)} \sum_{n=1}^{N(\lambda)} C_\lambda^{mn} T_\lambda^{mn}(g)$$

$$C_\lambda^{mn} = (2\lambda + 1) \int \exp[h(g)] T_\lambda^{mn}(g) \, \mathrm{d}g. \qquad (5.3.33)$$

The first OD approximation is now obtained by the positivity method described above (or the GHOST version as described in Van Houtte, 1983). Calling this latter $f_0(g)$, the first approximation for $h_0(g)$ is imposed as

$$h_0(g) = \begin{cases} \ln[f_0(g)] & \text{if } f_0(g) > \alpha, \\ f_0(g) - \alpha + \ln \alpha & \text{if } f_0(g) \leq \alpha. \end{cases}$$

An iterative refinement is carried out using

$$h_{k+1}(g) = h_k(g) + \sum_{\lambda=0}^{L} \sum_{m=1}^{M(\lambda)} \sum_{n=1}^{N(\lambda)} \exp[-h_k(g)](C_\lambda^{mn} - C_{\lambda,k}^{mn}) T_\lambda^{mn}(g).$$

C_λ^{mn} are the initial coefficients obtained by the positivity or GHOST method and the $C_{\lambda,k}^{mn}$ before each iteration are computed using (5.3.14b) and the $h_k(g)$ values of the OD. A normalization of $h_k(g)$ is performed at each step. At the end the always-positive OD is computed as $f(g) = \exp[h_k(g)]$.

5.3.2.3.9. *Radon transform and Fourier analysis*

The fundamental equation of QTA (5.3.11) can be recognized as the Radon transform (Radon, 1986) of $f(g)$ as proposed by Schaeben & van den Boogaart (2003),

$$\mathscr{R}f(\mathbf{h}, \mathbf{y}) = \frac{1}{2\pi} \int_{\tilde{\varphi}(\mathbf{h},\mathbf{y})} f(g) \, \mathrm{d}\tilde{\varphi}. \qquad (5.3.34)$$

The integration path $\tilde{\varphi}(\mathbf{h}, \mathbf{y})$ takes all of the equivalents of $\mathbf{h}$ into account, *i.e.* all of the rotations that represent the $\mathbf{h}$ multiplicity (such that $g\mathbf{h} = \mathbf{y}$). Because the Radon and the Fourier transforms are closely related, computationally efficient inversion formulas are available and $f(g)$ can be retrieved by fast Fourier inversion techniques. The biggest advantage is then that, unlike generalized spherical harmonics, both odd and even coefficients can be accessed from the inversion of the Radon transform.

5.3.2.4. *Inverse pole figures*

In a pole figure $P_\mathbf{h}(\mathbf{y})$ (5.3.11), all of the given $\mathbf{h}$ directions from all of the diffracting crystals are located using the $\mathbf{y}$ coordinates relative to K_A, the sample reference frame. In this way, one looks at only one of the equivalent $\mathbf{h}$ directions, and $\mathbf{y}$ varies in the pole figure. In some cases such as axially symmetric textures or when only some macroscopic directions $\mathbf{y}$ are of importance, it can be useful to represent which of the $\mathbf{h}$ directions align with the given $\mathbf{y}$. For instance, one can aim to see which crystal directions are aligned with a uniaxial pressure axis (σ). This time $\mathbf{y}$ is fixed (σ, or Z_A if the pressure is applied along Z_A) and $\mathbf{h}$ varies, and an easy way to represent such a distribution of $\mathbf{h}$ directions *versus* $\mathbf{y}$ is an inverse pole figure, or $R_\mathbf{y}(\mathbf{h})$. Similarly to (5.3.9), one can calculate every inverse pole figure $R_\mathbf{y}(\mathbf{h})$ from $f(g)$,

$$R_\mathbf{y}(\mathbf{h}) = \frac{1}{2\pi} \int_{\mathbf{y} \| \mathbf{h}} f(g) \, \mathrm{d}\tilde{\tilde{\varphi}}, \qquad (5.3.35)$$

in which $\tilde{\tilde{\varphi}}$ is an orientation path in $f(g)$ which takes account of the crystal symmetry. Inverse pole figures are represented in the crystal reference frame K_B (Fig. 5.3.6). Different sectors are equivalent by symmetry, from one for triclinic crystal symmetry to 24 for cubic symmetry. Only one sector is necessary to portray the unique information, and inverse pole figures are generally represented in the sector frame.

Similar to pole figures, inverse pole figures exhibit pole-density distributions. For instance, the inverse pole figure for the drawing axis of an aluminium wire shows that the $\langle 111 \rangle$ and $\langle 001 \rangle$ directions are the main alignment components, with a major $\langle 111 \rangle$
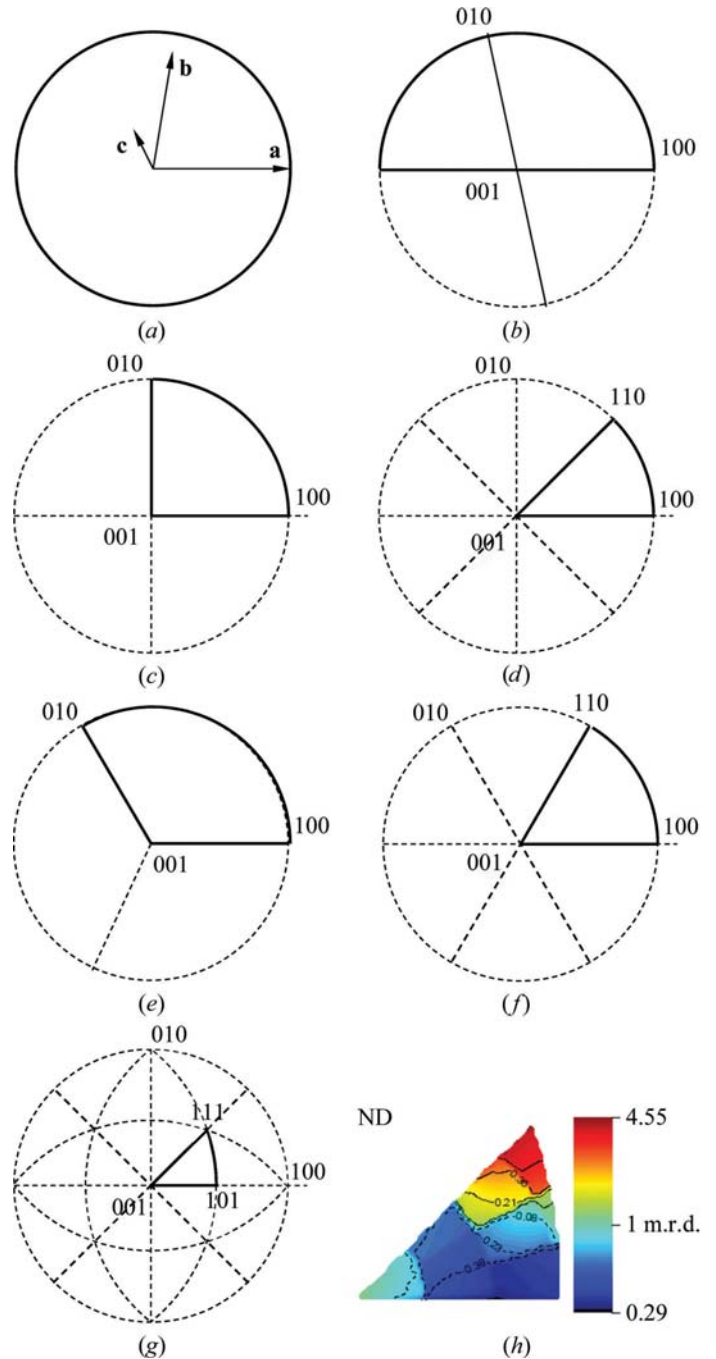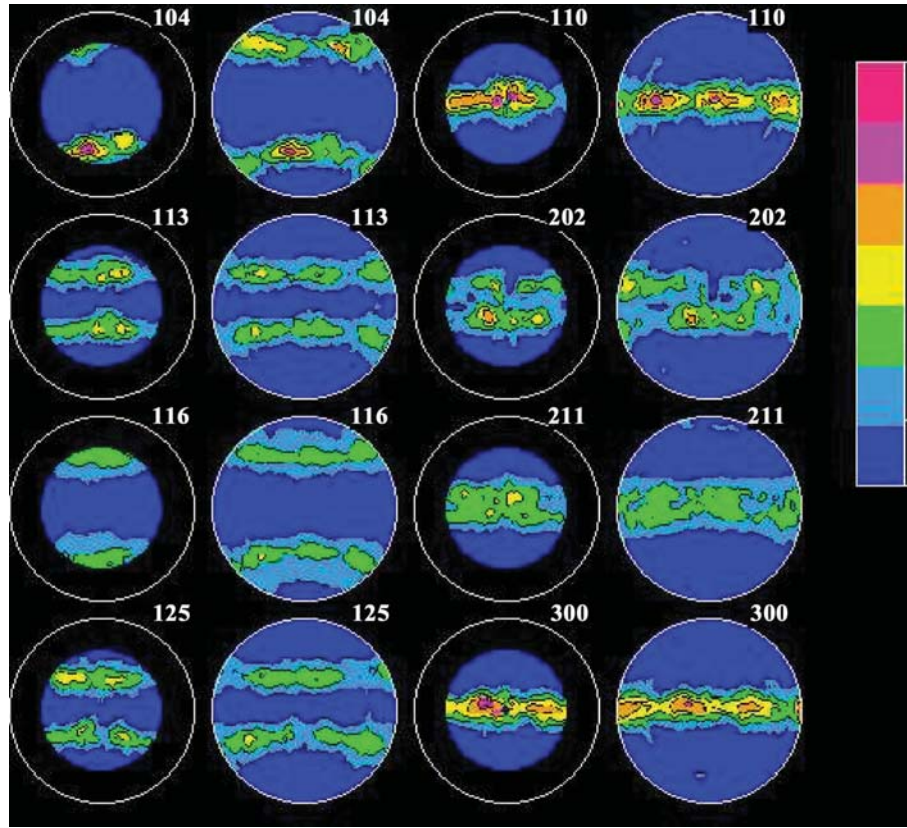

Figure 5.3.6
The inverse pole-figure sectors as a function of the crystal symmetry. The nonredundant sectors are indicated by bold edges. (*a*) Triclinic, (*b*) monoclinic (the *b*-axis unique setting has been used), (*c*) orthorhombic, (*d*) tetragonal, (*e*) rhombohedral using a hexagonal unit cell, (*f*) hexagonal and (*g*) cubic crystal systems. (*h*) An inverse pole figure for the drawing axis of an aluminium wire elaborated by cold drawing (linear density scale, cubic sector, equal-area projection).

Figure 5.3.7
Visual examination of the OD refinement reliability using experimental and recalculated normalized {104}, {110}, {113}, {202}, {116}, {211}, {125} and {300} pole figures (in successive order). WIMV refinements are from *BEARTEX*. Linear density scale, equal angular projections. The sample is the calcite outer prismatic layer of the deep-ocean mussel *Bathymodiolus thermophilus*, maximum density 6.3 m.r.d., minimum density 0 m.r.d. Here, $RP_{0.05} = 25\%$ and $RP_1 = 17\%$.

component, resulting from the gliding systems activated in the crystals (Fig. 5.3.6*h*).

5.3.2.5. *OD refinement reliability estimators*

As in Rietveld analysis, several factors are used to evaluate the reliability of the solution for $f(g)$. In most programs the RP_x factors are used,

$$\overline{RP}_x = \frac{1}{I} \sum_i \sum_j \frac{\left| P^c_{\mathbf{h}_i}(\mathbf{y}_j) - P^o_{\mathbf{h}_{ii}}(\mathbf{y}_j) \right|}{P^o_{\mathbf{h}_i}(\mathbf{y}_j)}, \qquad (5.3.36)$$

where $\mathbf{h}_i, i = 1, \ldots, I$, are the measured pole figures, $\mathbf{y}_j, j = 1, \ldots, J$, are the measured points of the pole figures, a superscript '*o*' indicates observed normalized values and a superscript '*c*' indicates recalculated normalized values, $P_{\mathbf{h}_i}(\mathbf{y}_j)$ is the pole density at $\mathbf{y}_j$ on pole figure $\mathbf{h}_i$, and $x = 0, \varepsilon, 1, 10, \ldots$ is the criterion to estimate the accuracy *versus* the density level.

The value x is a criterion that is used to indicate the quality of the refinement for the low- and high-density levels. We use $x = 0.05$ to reveal the global quality and $x = 1$ to show this quality for density values higher than 1 m.r.d. However, RP factors depend on the texture strength since they are not weighted by the density level, and consequently make the comparison of refinement quality between samples ambiguous (Chateigner, 2005). In other words, one should compare the refinement quality with RP factors only for similar texture strengths and types. Working out reliability factors on individual pole figures helps to detect whether some pole figures are particularly badly reproduced after the refinement, in order to devise a correction strategy.

In order to avoid texture-strength dependence of the reliability factors, surface-weighted factors (Matthies *et al.*, 1987) and several arithmetic mean averaging schemes have been described (Chateigner, 2005). Bragg-like factors also can be calculated, either weighted by density levels or not (Chateigner, 2005). However, using full patterns, Rietveld-like analysis provides 'intensity-weighted' factors, which exhibit less overall variation with texture strength and are better indicators for comparing OD refinement quality among samples,

$$Rw^z_x = \frac{\sum_{i=1}^{I} \sum_{j=1}^{J} \left[w^o_{ij} I^o_{\mathbf{h}_i}(\mathbf{y}_j) - w^c_{ij} I^c_{\mathbf{h}_i}(\mathbf{y}_j) \right]^2}{\sum_{i=1}^{I} \sum_{j=1}^{J} \left[w^z_{ij} I^z_{\mathbf{h}_i} \right]^2 (\mathbf{y}_j)} \theta[x, P^o_{\mathbf{h}_i}(\mathbf{y}_j)], \quad (5.3.37)$$

where

$$I^z_{\mathbf{h}_i}(\mathbf{y}_j) = P^o_{\mathbf{h}_i}(\mathbf{y}_j) N_{\mathbf{h}_i}$$

is the diffracted intensity, $N_{\mathbf{h}_i}$ is the refined normalizing factor,

$$w^z_{ij} = \frac{1}{[I^z_{\mathbf{h}_i}(\mathbf{y}_j)]^{1/2}}$$

is the diffracted intensity weight and

$$\theta(x, t) = \begin{cases} 1 & \text{for } P_{\mathbf{h}_i}(\mathbf{y}_j) > x, \\ 0 & \text{for } P_{\mathbf{h}_i}(\mathbf{y}_j) \leq x. \end{cases}$$

Whatever the reliability factors, one of the best estimates of a physically reasonable solution remains visual (Fig. 5.3.7). If the OD has been satisfactorily refined, any pole figure recalculated from this OD should compare well with the experimental pole figure.

563

5.3.2.6. Texture-strength factors

Once $f(g)$ has been satisfactorily obtained, some factors can give an estimate of the overall texture strength. These factors are used to compare samples with the same crystal symmetries and similar texture components.

5.3.2.6.1. Texture index

5.3.2.6.1.1. OD texture index

The first overall texture-strength parameter is the so-called 'texture index' (Bunge, 1982; expressed in units of m.r.d.[2]),

$$F^2 = \frac{1}{8\pi^2} \sum_i [f(g_i)]^2 \Delta g_i, \qquad (5.3.38)$$

where Δg_i is the OD cell volume. This index varies from 1 (random powder) to infinity (perfect texture or single crystal). It represents the mean-square value of the OD. Using harmonics, this factor is calculated from the C_λ^{mn} coefficients:

$$F^2 = 1 + \sum_{\lambda=2}^{L} \left(\frac{1}{2\lambda+1}\right) \sum_{m=-\lambda}^{\lambda} \sum_{n=-\lambda}^{\lambda} |C_\lambda^{mn}|^2. \qquad (5.3.39)$$

5.3.2.6.1.2. Pole-figure texture index

To compare the texture strengths of different samples, the texture index associated with given pole figures may be used,

$$J_{\mathbf{h}}^2 = \frac{1}{4} \sum_i [P_{\mathbf{h}}(\mathbf{y}_i)]^2 \Delta \mathbf{y}_i, \qquad (5.3.40)$$

with $\Delta \mathbf{y} = \sin\vartheta_{\mathbf{y}} \Delta\vartheta_{\mathbf{y}} \Delta\varphi_{\mathbf{y}}$.

5.3.2.6.2. Texture entropy

The second overall texture strength parameter is a measure of the texture disorder, evaluated by the calculation of the entropy (Shannon, 1948),

$$S = -\frac{1}{8\pi^2} \sum_i f(g_i) \ln f(g_i) \Delta g_i. \qquad (5.3.41)$$

5.3.2.6.3. Pole-figure and ODF strengths

Both OD and pole-figure indexes are expressed in units that are not homogeneous with distribution density units (m.r.d.). To help with comparison and interpretation, it is more convenient to compare the square roots of these values, *i.e.* the OD and pole-figure strengths, respectively (Kocks *et al.*, 1998),

$$F = (F^2)^{1/2} \text{ and } J_{\mathbf{h}} = (J_{\mathbf{h}}^2)^{1/2}. \qquad (5.3.42)$$

The texture entropy can also serve as another texture-strength definition, called F_S:

$$F_S = [\exp(-S)]^{1/2}. \qquad (5.3.43)$$

5.3.2.6.4. Correlation between F^2 and S

From the definitions of F^2 and S, their variations are restricted to the $(1, \infty)$ and $(0, -\infty)$ domains, respectively. Entropy and texture index are correlated, but it is not possible to obtain a general analytical expression for this correlation, which depends on $f(g)$. To appreciate it, one can represent $f(g)$ functions as points in the (F^2, S) plane. In this plane there is a lower bound for $f(g)$, which can be visualized by the $f(g)$ functions of strongly textured samples with no random component (Fig. 5.3.8). This lower bound for the H space (Hielscher *et al.*, 2007) is defined by
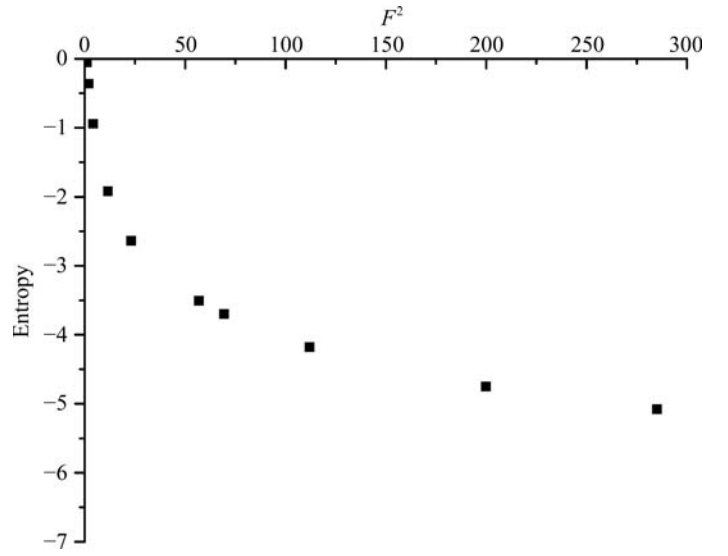

Figure 5.3.8
Entropy variation with texture index for modelled $f(g)$ functions.

$$S = -\ln F^2. \qquad (5.3.44)$$

No $f(g)$ function can be located below this bound, but *a priori* all of the space between it and the $S = 0$ axis of this graph corresponds to possible $f(g)$ functions. For instance, an OD composed of two components, one very sharp and corresponding to part of the sample volume and the other random and corresponding to the remaining volume fraction, would be positioned at the point $(300, -0.5)$. On the $S = 0$ axis only the point $(1, 0)$ corresponds to a valid point for $f(g)$, since if $S = 0$ then F^2 is automatically 1 m.r.d.[2].

5.3.2.7. Texture types

5.3.2.7.1. Random texture

A random texture (or random sample) belongs to the $\infty\infty/m$ Curie (limit) group and is simply a name given to the texture exhibited by a sample that has no preferred orientation. Its crystallites are randomly oriented. The same number of grains are diffracting at any $\mathbf{y}$, and the orientation density for any point $\mathbf{y}$ in a given $\mathbf{h}$ pole figure is the same. Consequently, all crystalline $\{hkl\}$ planes are randomly oriented, and $P_{\mathbf{h}}(\mathbf{y}) = 1$ m.r.d. for any $\mathbf{h}$ and $\mathbf{y}$, *i.e.* all pole figures exhibit homogeneous 1 m.r.d. densities. In such a texture, each crystallite has three degrees of freedom (rotations around three orthogonal axes) to orient K_B relative to K_A. Consequently, all of the OD values correspond to $f(g) = 1$ m.r.d. distribution densities, whatever the value of g.

However, in some samples only a fraction of the total volume, V_r, is randomly oriented; the rest, $V_c(g)$, is the oriented fraction volume with orientation component or components $f_c(g)$. The random part produces a background level in the OD, sometimes called 'fon' or 'phon', and one can decompose the OD as

$$f(g) = f_r + f_c(g), \qquad (5.3.45)$$

with the mandatory conditions $0 \leq f_r \leq 1$ and $f_r = \min[f(g)]$.

By integrating (5.3.1) and taking into account (5.3.35), one obtains

$$\frac{V_r + V_c(g)}{V} \frac{1}{8\pi^2} \oint [f_r + f_c(g)] \, dg,$$
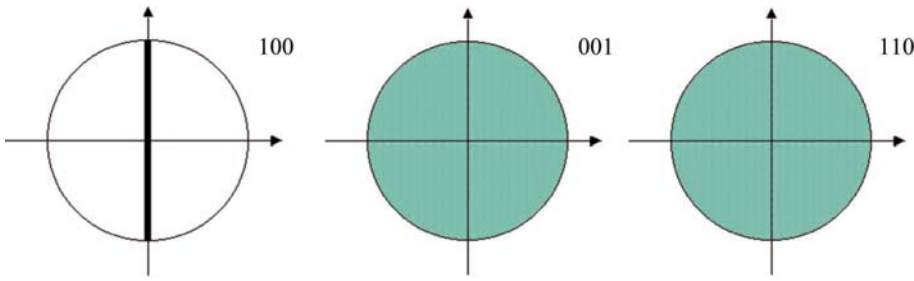
which verifies that

Figure 5.3.9
{100}, {001} and {110} pole figures of a planar texture in an orthorhombic crystal system. The rotation axis of the planar texture is with $\langle 100\rangle^*$ directions perpendicular to X_A.
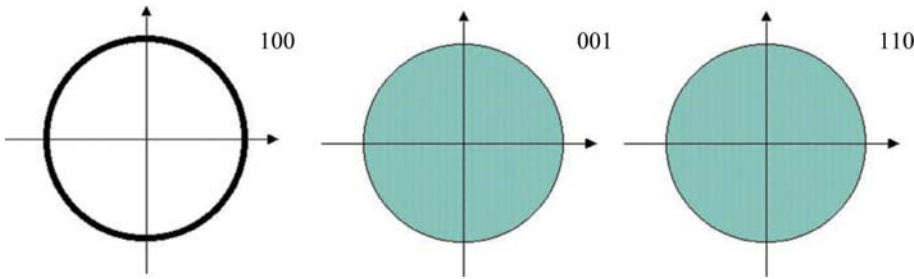

Figure 5.3.10
{100}, {001} and {110} pole figures of a cyclic-planar texture in an orthorhombic crystal system. The rotation axis of the cyclic-planar texture is with $\langle 100\rangle^*$ directions perpendicular to Z_A.
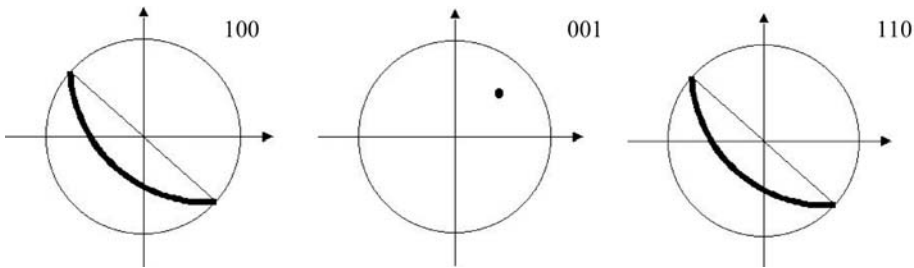

Figure 5.3.11
{100}, {001} and {110} pole figures of a fibre texture in an orthorhombic crystal system. The fibre axis is with $\langle 001\rangle^*$ directions at ($\vartheta_{\mathbf{y}} = 45°$, $\varphi_{\mathbf{y}} = 45°$).
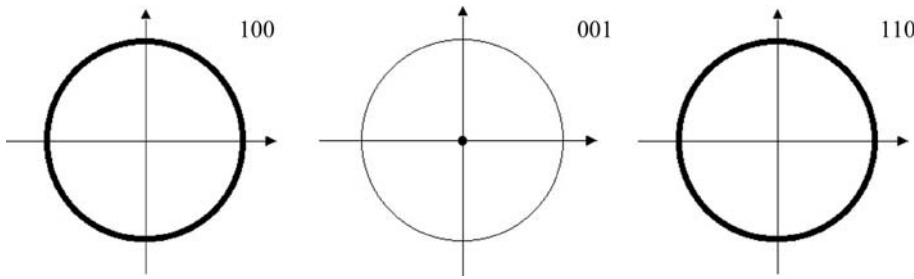

Figure 5.3.12
{100}, {001} and {110} pole figures of a cyclic-fibre texture in an orthorhombic crystal system. The fibre axis is with $\langle 001\rangle^*$ directions along Z_A.
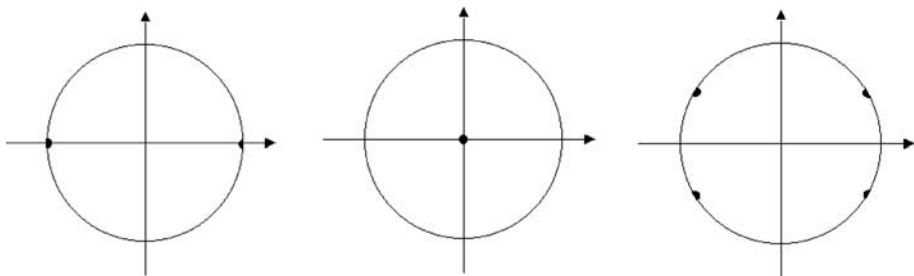

Figure 5.3.13
{100}, {001} and {110} pole figures of a three-dimensional texture in an orthorhombic crystal system, with $\langle 001\rangle^*$ directions along Z_A and $\langle 100\rangle^*$ directions along X_A.

$V_r/V = f_r$ for the random part, and

$$\frac{dV_c(g)}{V} = \frac{1}{8\pi^2} f_c(g)\, dg \quad \text{for the textured part.}$$

$$(5.3.46)$$

This strictly means that the minimum value of the OD (e.g. $f_r = 0.3$ m.r.d.) defines the random volume fraction, i.e. 30% of the material is randomly oriented in this case.

5.3.2.7.2. Planar textures

This kind of texture is exhibited by samples in which the crystallites have two degrees of freedom to orient and belong to the $\infty\infty$ Curie group. One specific $\langle hkl\rangle^*$ direction family is allowed to rotate around one sample axis. The $\langle hkl\rangle^*$ directions are then located at random in a K_A plane perpendicular to the rotation axis. For instance, if the rotation axis is X_A with the direction family $\langle 100\rangle^*$ of an orthorhombic crystal system (Fig. 5.3.9), the the $\langle 100\rangle^*$ directions are then distributed in the (Y_A, Z_A) plane. However, since the other directions are at random around $\langle 100\rangle^*$, their pole figures remain quite homogeneous.

Of course, it is a special case that the rotation axis is along a major axis of the sample, and that the $\langle 100\rangle^*$ (**a** axes) are the directions concerned. There could have been an inclined axis of rotation and reflections with a larger multiplicity, giving rise to more complex pole figures. Planar textures with the rotation axis around Z_A are called a 'cyclic-planar' texture (Fig. 5.3.10).

5.3.2.7.3. Fibre textures

If the crystallites lose another degree of freedom in their orientation (∞, ∞m, ∞/m, $\infty 2$ or ∞/mm Curie groups), they are forced to align one of their $\langle hkl\rangle^*$ directions with one direction **y** of K_A, with all other directions being at random around $\langle hkl\rangle^*$. Such a texture is called 'fibre texture'. For instance, if all of the $\langle 001\rangle^*$ directions from an orthorhombic crystal system are located along **y** = ($\vartheta_{\mathbf{y}} = 45°$, $\varphi_{\mathbf{y}} = 45°$) (Fig. 5.3.11), then the $\langle 100\rangle^*$ and $\langle 110\rangle^*$ directions will be located at random in a plane perpendicular to this **y**. As above, if the $\langle 001\rangle^*$ directions are aligned with Z_A then the texture is called a 'cyclic-fibre' texture (Fig. 5.3.12). Such a texture has the $\langle 100\rangle^*$ and $\langle 110\rangle^*$ poles located on the periphery of the pole figures.

5.3.2.7.4. Three-dimensional textures

Samples composed of crystallites which have had no opportunity to orient themselves in K_A (zero degrees of freedom) will exhibit point poles for all of their pole figures. The pole figures will be similar to those of a single crystal. We call this a 'three-dimensional' or 'single-crystal-like' texture. For instance if the
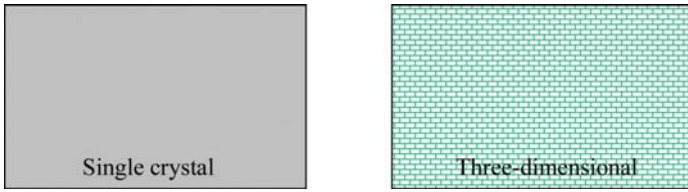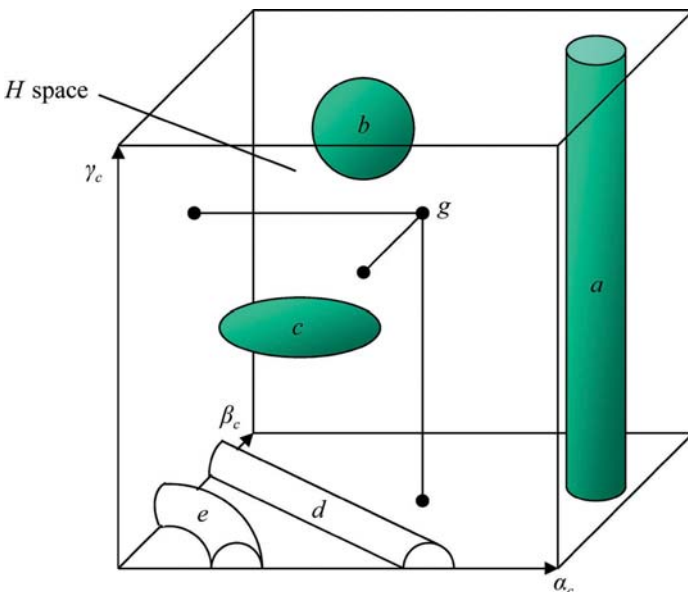
Figure 5.3.14
The difference between a perfect single crystal and a polycrystal with perfect three-dimensional crystallite orientations. The normalized pole figures should be identical.

$\langle 001 \rangle$* directions are aligned with Z_A and the $\langle 100 \rangle$* directions with X_A, the pole figures will look like those in Fig. 5.3.13, and the φ_y angles to which the $\langle 110 \rangle$* poles are localized will depend on the b/a ratio of the orthorhombic structure.

One should avoid confusion between real single crystals and polycrystals exhibiting three-dimensional textures (Fig. 5.3.14). A single crystal, as usually understood in single-crystal crystallography, exhibits a 'mosaicity', itself composed of a mosaic spread and size. The mosaic spread is often measured using a so-called 'rocking curve', *i.e.* a limited view of the complete texture, and in this sense is a 'three-dimensional texture' with very small crystallite misorientation. The mosaic size represents the coherent domains (crystallites) of the mosaic in the single crystal. A perfect three-dimensional texture can correspond either to an ensemble of coherent domains with respective crystal reference frames perfectly parallel to one another (*i.e.* with no spread) but with no wave coherence between them, or to a large single crystal that diffracts as a single coherent domain. The diffracted intensity is much larger in the latter case and the direct pole figures will show very large intensities compared with the former. However, the normalized pole figures will be the same in both cases, as all effects other than crystal orientation are eliminated by normalization.

5.3.2.7.5. *Typical OD components*

Each of the previous texture types has corresponding OD descriptions as components of orientations, which can be repre-

Figure 5.3.15
Isodensity surfaces representing isolated OD components in a Cartesian coordinate system in *H* space.
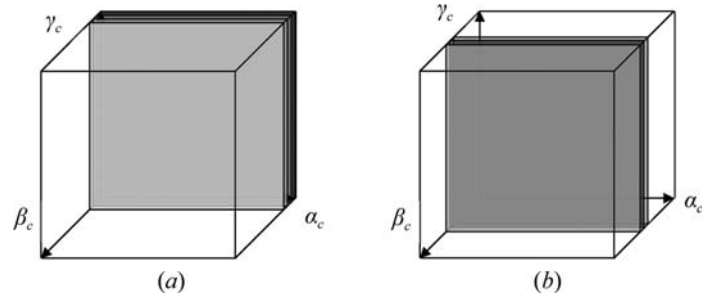
Figure 5.3.16
Several isodensity surfaces representing a cyclic-fibre OD (*a*) and a cyclic-planar OD (*b*) in *H* space.

sented, for example, using a Cartesian coordinate system for *H* space (Fig. 5.3.15) and isodensity surfaces for simplicity. An individual point *g* in this space represents an individual orientation located at $\{\alpha_c, \beta_c, \gamma_c\}$. A spherical component (*b* in Fig. 5.3.15) consists of concentric spheres with increasing radii for lower densities, with the level of these latter depending on the choice of the function representing the component. An elliptical component (*c*) shows an elongation in one or two directions (here along the α_c rotation axis). A tube around a given (α_c, β_c) couple that is elongated over the whole γ_c range represents a fibre texture with a fibre axis that is inclined with respect to the main K_A axis (*a* in Fig. 5.3.15). Isolated components respecting specific relationships between their coordinates can also exist; for instance, a tube around $\gamma_c = 0$ with $\alpha_c + \beta_c =$ constant (*d* in Fig. 5.3.15) or $\alpha_c^2 + \beta_c^2 =$ constant (*e* in Fig. 5.3.15).

For cyclic-fibre components $\beta_c = 0$ and α_c is distributed on 2π. In this configuration, a γ_c rotation or an α_c rotation have the same effect and the whole (α_c, γ_c) plane is filled by density (Fig. 5.3.16*a*). In a cyclic-planar texture (Fig. 5.3.16*b*), on the contrary, $\beta_c = 90°$. However, in this case both α_c and γ_c are distributed on 2π, since the cyclic-planar axis Z_B is distributed in the (X_A, Y_A) plane and since all directions are at random Z_B. The result is an ODF representation that looks very similar to that of a cyclic-fibre texture, except for the coordinate of the high density levels along the β_c axis of rotation.

5.3.2.8. *Reciprocal-space mapping*

Reciprocal-space mapping (RSM) represents the localization of the momentum transfer in the sample reference frame (K_A). The momentum-transfer vector **q** is defined by

$$\mathbf{q} = (\mathbf{k}_o - \mathbf{k}_i),$$
$$\|\mathbf{q}\| = \frac{4\pi}{\lambda} \sin \theta = 2\|\mathbf{k}\|, \tag{5.3.47}$$

in which $\mathbf{k}_i$ and $\mathbf{k}_o$ are the incident and outgoing wavevectors, respectively. The goal of RSM is then to locate a reciprocal vector, defined in reciprocal space **R**, in a reference frame defined in the sample direct space. Since **q** is perpendicular to the diffracting plane (*hkl*), it is also parallel to the normal **h** of this latter. Consequently, RSM first determines the ensemble of $I_\mathbf{h}(\mathbf{y})$ diffracted intensities for the **y** orientations of a given reciprocal node corresponding to the extension of the Bragg peak **h** on the pole sphere. At this point one should notice that RSM is generally performed on strongly oriented samples such as epitaxial layers or single crystals. Each **y** set of measured orientations is then restricted in sample space on the pole sphere for a given **h**. However, this does not avoid the measurement of a large number

of points for each **h** to correctly describe the reciprocal-space node.

Secondly, one has to transform measured **y** directions of Y space to their corresponding values in R by multiplying them by the norm $\|\mathbf{q}\|$ of the **q** vector. This results in a set of $I_\mathbf{h}(\mathbf{q})$ values represented in K_A.

From the pole-figure definitions, the **q** coordinates are

$$q_{X_A} = \frac{4\pi}{\lambda} \sin\theta \sin\vartheta_\mathbf{y} \cos\varphi_\mathbf{y}$$

$$q_{Y_A} = \frac{4\pi}{\lambda} \sin\theta \sin\vartheta_\mathbf{y} \sin\varphi_\mathbf{y}$$

$$q_{Z_A} = \frac{4\pi}{\lambda} \sin\theta \cos\vartheta_\mathbf{y}. \qquad (5.3.48)$$

5.3.3. Magnetic quantitative texture analysis (MQTA)

5.3.3.1. *Magnetization curves and magnetic moment distributions*

The measurement of magnetic pole figures using neutron diffraction is sparsely documented and only a few attempts at refining magnetic ODs have been carried out to date (Birsan *et al.*, 1996), although knowledge of the anisotropic distribution of magnetic moments in a sample has been shown to be of crucial importance to predict macroscopic magnetic behaviours (Morales *et al.*, 2003). Anisotropic magnetic behaviour is usually probed using magnetization curves measured in only two perpendicular macroscopic directions of the sample, and is then intrinsically subjected to strong biases if the sample magnetic moment distribution does not respect some symmetry, adapted to the magnetization measurement (Fig. 5.3.17). Magnetic moment distribution characterization is thus a prerequisite for checking the validity of magnetization measurements for a given sample-measurement configuration.

Neutron diffraction is perfectly suited for the examination of macroscopic magnetic moment distributions, provided that one can measure the same sample with and without the application of an external magnetic field during the measurements (Chateigner *et al.*, 2010).

5.3.3.2. *Magnetic pole figures and magnetic ODs*

5.3.3.2.1. *Magnetic pole figures and ODs*

Using neutron diffraction, pole figures are composed of a nuclear (n; the usual crystallographic pole figures) and a magnetic (m) part in zero field or under the application of an external magnetic field **B**,
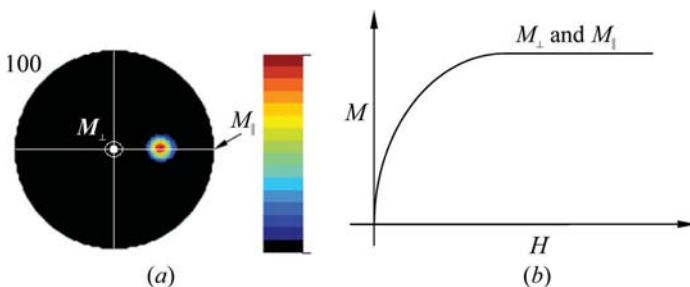

Figure 5.3.17
Illustration of a case for which a magnetization measurement in two perpendicular directions cannot reveal the macroscopic magnetic anisotropy. (*a*) Virtual distribution of the magnetic moments, with magnetic moments at 45° from both magnetization measurement directions, and (*b*) the corresponding magnetization curves.

$$I_\mathbf{h}(\mathbf{y}) = I_\mathbf{h}^n(\mathbf{y}) + I_\mathbf{h}^m(\mathbf{y}),$$

$$I_\mathbf{h}(\mathbf{y}, \mathbf{B}) = I_\mathbf{h}^n(\mathbf{y}, \mathbf{B}) + I_\mathbf{h}^m(\mathbf{y}, \mathbf{B}). \qquad (5.3.49)$$

For crystallites that are not free to rotate under **B**, for example in the solid state without phase transformation,

$$I_\mathbf{h}^n(\mathbf{y}, \mathbf{B}) = I_\mathbf{h}^n(\mathbf{y}), \quad \text{hence}$$

$$I_\mathbf{h}(\mathbf{y}, \mathbf{B}) = I_\mathbf{h}^n(\mathbf{y}) + I_\mathbf{h}^m(\mathbf{y}, \mathbf{B}). \qquad (5.3.50)$$

This latter equation is of interest because it can serve for the determination of the magnetic part from an independent determination of the nuclear part, for example using X-ray diffraction. The application of a field **B** eventually induces a reorientation of magnetic moments in the sample, or magnetic polarization, which is seen using neutron diffraction as variations of intensities, $\Delta I_\mathbf{h}^m(\mathbf{y}, \mathbf{B})$, in the pole figures, and (5.3.49) becomes

$$I_\mathbf{h}(\mathbf{y}, \mathbf{B}) = I_\mathbf{h}^n(\mathbf{y}, \mathbf{B}) + I_\mathbf{h}^m(\mathbf{y}, 0) + \Delta I_\mathbf{h}^m(\mathbf{y}, \mathbf{B}). \qquad (5.3.51)$$

As for crystallographic QTA, total magnetic scattering normalized pole figures [$P_\mathbf{h}^m(\mathbf{y}, \mathbf{B})$], normalized magnetic scattering polarization pole figures [$\Delta P_\mathbf{h}^m(\mathbf{y}, \mathbf{B})$] and their respective magnetic ODs [$f_m(g, \mathbf{B})$ and $f_m^p(g, \mathbf{B})$] have to respect normalization with their respective normalization factors (random intensities),

$$\int\limits_\mathbf{y} P_\mathbf{h}^m(\mathbf{y}, \mathbf{B}) \, d\mathbf{y} = 2\pi,$$

$$\int\limits_\mathbf{y} \Delta P_\mathbf{h}^m(\mathbf{y}, \mathbf{B}) \, d\mathbf{y} = 0,$$

$$I_\mathbf{h}^{n,r} = \frac{\int_\mathbf{y} I_\mathbf{h}^n(\mathbf{y}, \mathbf{B}) \, d\mathbf{y}}{\int_\mathbf{y} d\mathbf{y}},$$

$$I_\mathbf{h}^{m,r} = \frac{\int_\mathbf{y} I_\mathbf{h}^m(\mathbf{y}, \mathbf{B}) \, d\mathbf{y}}{\int_\mathbf{y} d\mathbf{y}} = I_\mathbf{h}^{m,r}(\mathbf{y}, 0) = I_\mathbf{h}^{m,r}(\mathbf{y}, \mathbf{B}),$$

$$\int\limits_g f_m(g) \, dg = 4\pi^2,$$

$$\int\limits_g f_m^p(g) \, dg = 0. \qquad (5.3.52)$$

5.3.3.2.2. *Fundamental equations of MQTA*

Since two different magnetic scattering pole figures and ODs have been constructed, there are two corresponding fundamental equations:

$$P_\mathbf{h}^m(\mathbf{y}, \mathbf{B}) = \frac{1}{2\pi} \int\limits_{\mathbf{h}\|\mathbf{y}} f_m(g, \mathbf{B}) \, d\tilde{\varphi} \qquad (5.3.53)$$

for the total magnetic scattering, with $\tilde{\varphi}$ in general different from that of the crystallographic (nuclear) part since magnetic and nuclear cells can have different rotation groups, and

$$\Delta P_\mathbf{h}^m(\mathbf{y}, \mathbf{B}) = \frac{1}{2\pi} \int\limits_{\mathbf{h}\|\mathbf{y}} f_m^p(g, \mathbf{B}) \, d\tilde{\varphi} \qquad (5.3.54)$$

for the polarization part. Because the normalization of the polarization part requires us to work in the 'positive' and 'negative' spaces of the polarization pole figures, this latter equation is in fact composed of two parts:
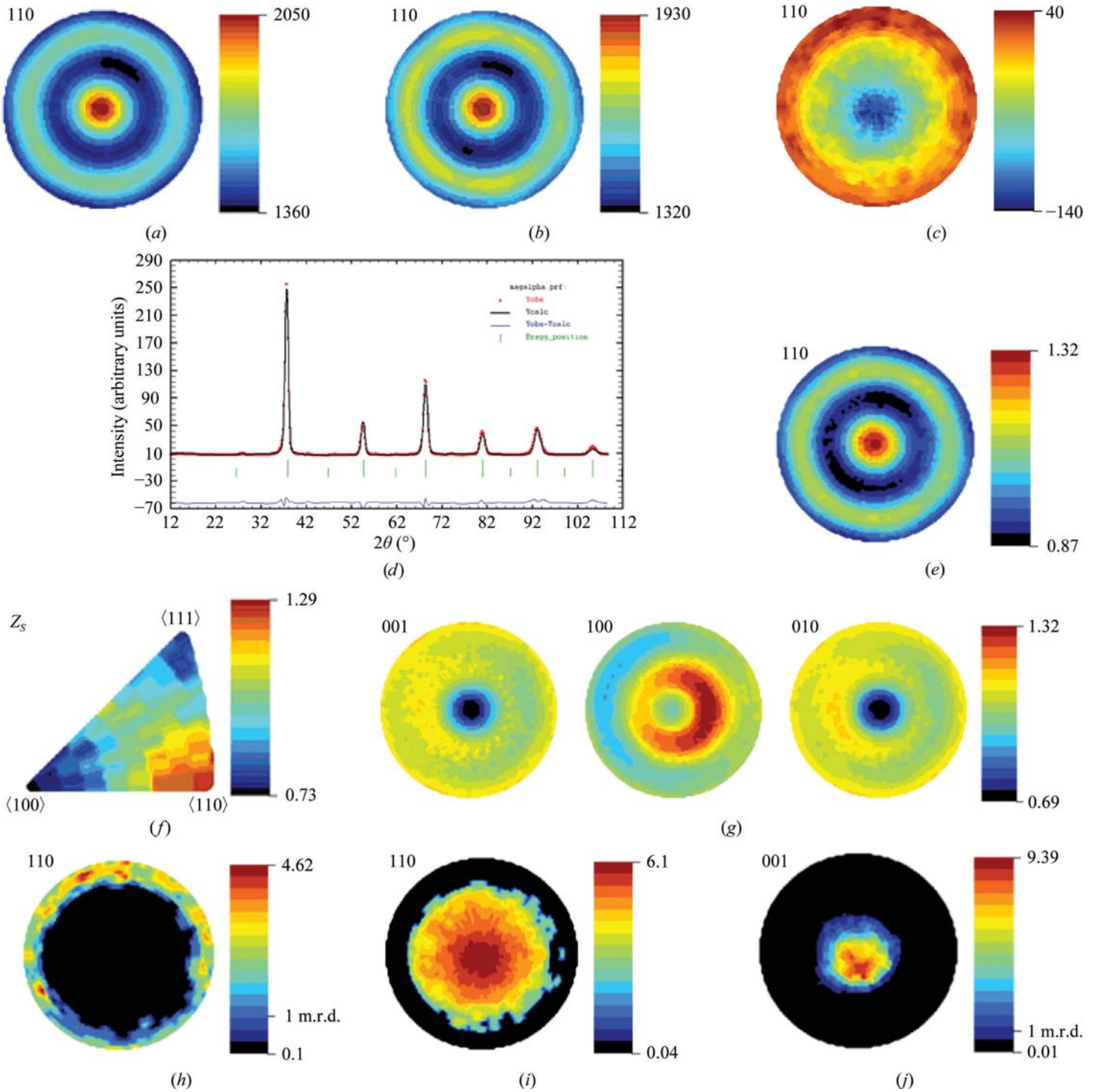
Figure 5.3.18

{110} pole figures at zero field (*a*), under 0.3 T (*b*) and the difference (*c*). (*d*) Fit of the sum of all diagrams at zero field using the orthorhombic magnetic subgroup in *FullProf*; (*e*) WIMV recalculated/normalized nuclear {110} pole figure. (*f*) Inverse nuclear pole figure for the cylinder sample-axis direction and (*g*) WIMV recalculated/normalized magnetic scattering contribution for the main orthorhombic axes. (*h*–*j*) Recalculated/normalized magnetic scattering polarization pole figures for the positive (*h*) and negative (*i*) parts of the difference pole figures, and the corresponding positive {001} magnetic scattering pole figure illustrating the magnetic moment reorientation (*j*).

$$\Delta P_{\mathbf{h}}^{m+}(\mathbf{y}, \mathbf{B}) = \frac{1}{2\pi} \int_{\mathbf{h} \parallel \mathbf{y}} f_m^{p+}(g, \mathbf{B}) \, \mathrm{d}\tilde{\varphi},$$

$$\Delta P_{\mathbf{h}}^{m-}(\mathbf{y}, \mathbf{B}) = \frac{1}{2\pi} \int_{\mathbf{h} \parallel \mathbf{y}} f_m^{p-}(g, \mathbf{B}) \, \mathrm{d}\tilde{\varphi}. \qquad (5.3.55)$$

The correct normalizations and determinations of the various orientation quantities accessible to neutron diffraction depend on many factors. The possibilities of observing neutron peaks without magnetic contributions and the initial magnetic and crystallographic orientation states of the sample (isotropic or anisotropic) have been discussed elsewhere (Chateigner *et al.*, 2010).

5.3.3.3. *An example*

Here, we illustrate magnetic quantitative texture analysis on an iron sample exhibiting magnetic saturation around 0.5 T (Chateigner *et al.*, 2010) that was initially not magnetized. Measurements were carried out on the D19 beamline at ILL first without and then with an applied magnetic field of 0.3 T, which is

sufficient to partly reorient the magnetic moments. At zero field (Fig. 5.3.18a) the sample exhibits a strong signal with a moderate ⟨110⟩ crystallographic texture. Under a 0.3 T field (Fig. 5.3.18b), the maximum of the {110} experimental pole figure decreases significantly at the benefit of the pole-figure equator. This is coherent with a magnetic field applied along the sample cylinder axis (Z_A), with which magnetic moments tend to align, giving rise to more magnetic diffraction signal 90° to it. The difference {110} pole figure illustrates this more explicitly (Fig. 5.3.18c), with negative differences at its centre and positive values on its equator. We then calculated the random magnetic contribution of the isotropic magnetic sample using *FullProf* (Fig. 5.3.18d), using the sum of all diagrams measured at all of the sample orientations, taking into account the resolution characteristics of the D19 instrument. This random magnetic contribution provides the possibility of decoupling nuclear and magnetic contributions at zero field: $I_h^n(\mathbf{y}, 0)$ and $I_h^m(\mathbf{y}, 0)$, respectively (Chateigner *et al.*, 2010). These latter pole figures were used to refine the corresponding ODs, $f_n(g)$ and $f_m(g)$, using the body-centred cubic crystal symmetry and the orthorhombic magnetic symmetries, respectively, and the WIMV algorithm in *BEARTEX* (Wenk *et al.*, 1998). The nuclear ⟨110⟩ fibre texture (Fig. 5.3.18e) culminates at 1.32 m.r.d. [$f_n^{\max}(g)$ = 1.8 m.r.d., $f_n^{\min}(g)$ = 0.61 m.r.d., F^2 = 1.03 m.r.d.^{2}, RP$_0$ = 1.42%], and the fibre axis is aligned with Z_A as the sole textured component (Fig. 5.3.18f). Since the easy-axis direction for magnetization in iron is ⟨100⟩, the actual ⟨110⟩ fibre does not correspond to an easy-magnetization configuration. Consequently, the total normalized magnetic scattering pole figures of the main magnetic unit-cell axes (Fig. 5.3.18g) do not show a strong reorientation of densities, and exhibit a maximum of only 1.32 m.r.d. on the pole figures, but a larger OD maximum value [$f_n^{\max}(g)$ = 2.3 m.r.d., $f_n^{\min}(g)$ = 0.64 m.r.d., F^2 = 1.03 m.r.d.^{2}, RP$_0$ = 0.24%].

From the magnetic scattering polarization pole figures we refined the magnetic polarization OD, $f_m^{p+}(g)$ and $f_m^{p-}(g)$. Since the magnetic scattering difference pole figures show positive and negative values, we divided them into positive and negative zones, $\Delta I_h^{m+}(\mathbf{y}, \mathbf{B})$ and $\Delta I_h^{m-}(\mathbf{y}, \mathbf{B})$, respectively, assigning zeros to the negative cells of $\Delta I_h^{m+}(\mathbf{y}, \mathbf{B})$ and *vice versa*. From $\Delta I_h^{m+}(\mathbf{y}, \mathbf{B})$ and $|\Delta I_h^{m-}(\mathbf{y}, \mathbf{B})|$ we refined the magnetic scattering polarization ODs, $f_m^{p+}(g)$ [$f_m^{p+,\max}(g)$ = 93 m.r.d., $f_m^{p+,\min}(g)$ = 0 m.r.d., F^2 = 12.4 m.r.d.^{2}, RP$_0$ = 6.83%] and $f_m^{p-}(g)$ [$f_m^{p-,\max}(g)$ = 6.1 m.r.d., $f_m^{p-,\min}(g)$ = 0.04 m.r.d., F^2 = 2.70 m.r.d.^{2}, RP$_0$ = 0.00%] in *BEARTEX*, which yielded the normalized $\Delta P_{110}^{m+}(\mathbf{y}, \mathbf{B})$ and $|\Delta P_{110}^{m-}(\mathbf{y}, \mathbf{B})|$ pole figures (Figs. 5.3.18h and 5.3.18i, respectively). These latter clearly show the reoriented part of the magnetic signal, with a large density created in the centre of $|\Delta P_{110}^{m-}(\mathbf{y}, \mathbf{B})|$, indicating a departure of intensities in this area to reach the periphery of $\Delta P_{110}^{m+}(\mathbf{y}, \mathbf{B})$, both pointing towards magnetic moment alignment with Z_A. The maximum densities observed in these latter pole figures measure the strength of the intensity reorientations, as also seen from the texture indexes and OD maxima. Most importantly, since the diffracted signal reveals magnetic moments that are located 90° to it, one can search in this case for a reflection at this angle from [110], which is, for instance, 001 in this space group. The $\Delta P_{110}^{m+}(\mathbf{y}, \mathbf{B})$ (Fig. 5.3.18j) then directly reveals the distribution of reoriented magnetic moments, which in this case indicates a 9.4 m.r.d. density of reorientation. Interestingly, in this case one can see a slight but significant deviation of these magnetic moments with respect to Z_A (⟨110⟩ crystallographic fibre axis), probably owing to difficulty in controlling the application of the magnetic field.

5.3.4. Modelling of preferred orientation in the Rietveld method

The modelling of preferred orientation in diffraction patterns was originally developed to facilitate structure determination. The presence of an unrecognized preferred orientation can be fatal to structure solution. Texture is particularly present in easily cleaved materials or materials with anisotropic habits, and when the samples are prepared by anisotropic techniques. X-ray diffraction specimen preparation often introduces preferred orientations, which have been mostly considered as an undesirable phenomenon in Rietveld analysis.

When textures have not been removed successfully by careful grinding and packing, the remaining texture has to be modelled during the analysis. There are two types of texture treatments in Rietveld analysis. If the texture is simple (smooth, fibre type and not too severe), it can be modelled using analytical formulae. If it is more complex (several texture components, sharp pole figures) the treatment requires a quantitative texture analysis (the subject of Section 5.3.2). In this section the simplest texture corrections are described, but the best way to characterize texture effects is to carry out QTA inside the Rietveld approach. The texture is roughly modelled using three parameters:

 (i) a texture axis linked to the sample symmetry (the normal to the sample surface for a flat sample in Bragg–Brentano geometry or the cylinder axis in Debye–Scherrer geometry),
 (ii) the crystallographic direction **h**, which tends to align with the previous axis, and
 (iii) a texture strength (angular dispersion, texture factor *etc.*).

5.3.4.1. *Rietveld and March approaches*

The preferred orientations are modelled in the original equation of Rietveld by the March function (March, 1932) using the function $P_\mathbf{h}$,

$$P_\mathbf{h} = \exp(-G_1 \alpha_\mathbf{h}^2) \tag{5.3.56}$$

or

$$P_\mathbf{h} = G_2 + (1 - G_1)\exp(-G_1 \alpha_\mathbf{h}^2), \tag{5.3.57}$$

where G_1 and G_2 are refinable parameters and $\alpha_\mathbf{h}$ is the angle between the texture direction **h** and the scattering vector.

5.3.4.2. *March–Dollase approach*

Dollase proposed an improvement to the March approach using the following function (Dollase, 1986):

$$P_\mathbf{h} = \left[G_1^2 \cos^2 \alpha_\mathbf{h} + \left(\frac{1}{G_1} \right) \sin^2 \alpha_\mathbf{h} \right]^{-3/2}. \tag{5.3.58}$$

Originally, the March correction assumed a Gaussian distribution of the preferred-orientation axis of the individual crystallites about an axis. G_1 is a refinable parameter that now controls the distribution shape and is an index of the preferred-orientation strength ($0 < G_1 \leq 1$; $G_1 = 1$ for a random orientation).

This model provides
 (i) a preferred-orientation model with minimum or maximum at $\alpha_\mathbf{h} = 0°$,
 (ii) a symmetric and smooth evolution in the (0, 90°) $\alpha_\mathbf{h}$ range,
 (iii) a single parameter to be fitted, and

(iv) the possibility of normalization of the orientation,

$$\int_0^{\pi/2} P_{\mathbf{h}} \sin \alpha_{\mathbf{h}} \, d\alpha_{\mathbf{h}} = 1. \tag{5.3.59}$$

This latter property is important in order to keep the total diffracted intensity in a diffraction diagram constant whatever the distribution shape $P_{\mathbf{h}}$. A point that is often not realized is that the March–Dollase approach assumes cylindrical sample symmetry.

5.3.4.3. Modified March–Dollase models

More recently, Brosnan *et al.* (2006) proposed a modification of the March–Dollase approach by including a 'random' orientation factor,

$$P_{\mathbf{h}} = f \left\{ \left[G_1^2 \cos^2 \alpha_{\mathbf{h}} + \left(\frac{1}{G_1} \right) \sin^2 \alpha_{\mathbf{h}} \right]^{-3/2} \right\} + (1 - f). \tag{5.3.60}$$

In this model, it is expected that the factor f provides the random part, *i.e.* the volume of randomly oriented crystallites. However, it must be noted that this factor is linked to the component of orientation that is described by the formula. Since this only describes one orientation component, *i.e.* a specific $\mathbf{h}$ distributed in a given distribution around the normal to the sample, f is in fact only the volume fraction of crystallites that have their $\mathbf{h}$ direction in this distribution component, with $(1 - f)$ being the volume fraction of crystallites that are not in this component (oriented differently) but are not necessarily randomly oriented. Let us give an example to illustrate this point: imagine a sample containing tetragonal crystallites with a single orientation component, for example with their c axes distributed in a Gaussian around the normal. In this case, if $f = 0.5$, 50% of the crystallites have [001] directions inside the Gaussian component. However, there is no information, for instance, about the orientation of the a axes around the orientation component. Thus, $(1 - f)$ does not mean that 50% of the crystallites are necessarily randomly oriented; the a axes may possibly be strongly oriented along one specific direction in the plane perpendicular to the c axes. The parameter f hence does not represent the orientation distribution function $f(g)$, and one should not confuse them.

A second modification (Zolotoyabko, 2009) focuses on the estimation of an orientation degree parameter η_Z, defined on the basis of the Dollase parameter G_1:

$$\eta_Z (\%) = \left[\frac{(1 - G_1)^3}{1 - G_1^3} \right]^{1/2}. \tag{5.3.61}$$

The η_Z parameter tends to zero as G_1 values reach 1 and to 100% for $G_1 = 0$. It can easily be introduced in Rietveld programs and intrinsically contains the normalization condition of (5.3.59).

5.3.4.4. Donnet–Jouanneaux function

This model for preferred orientation is purely empirical, with a parameter D controlling the preferred orientation ($D = 0$ for a random orientation) (Jouanneaux, 1999):

$$P_{\mathbf{h}} = 1 + \frac{D \cos 2\alpha_{\mathbf{h}}}{1 + (G - 1) \sin^2 \alpha_{\mathbf{h}}}. \tag{5.3.62}$$

5.3.4.5. Modelling by spherical harmonics (and exponential)

Järvinen and others (Ahtee *et al.*, 1989; Järvinen, 1993) initially proposed the use of a harmonic method to model preferred orientation in Rietveld refinement for cylindrical sample symmetry. The idea was expanded by Popa (1992) to all sample symmetries and implemented by Von Dreele in *GSAS* (Larson & Von Dreele, 2000).

Equation (5.3.13) is utilized to compute the preferred-orientation effect on intensities as a function of the coefficients. The sample symmetry must be imposed depending on the kind of measurement that is performed. In general, with only one pattern in either Bragg–Brentano or Debye–Scherrer geometry, a cylindrical symmetry (fibre texture) for the sample should be used. The fibre axis will be normal to the surface of the sample for the Bragg–Brentano case and along the capillary axis for the Debye–Scherrer case. Spinning the sample along this fibre axis will ensure the correct symmetry for the sample in cases where it is not correct. When a static specimen with known rolling or shear texture is measured (preferably in multiple orientations), the appropriate noncylindrical sample symmetry should be used, and the angles relating the different orientations must be considered.

Another remark should be made on the use of spherical harmonics with the Rietveld method. All spherical-harmonics descriptions and implementations (the same is also true for discrete methods such as WIMV, EWIMV and ADC) in the case of monoclinic crystal symmetry work only in the c-axis unique (Mattheis & Wenk, 2009) setting.

Different approaches have been used to ensure an OD that is always positive. The approaches used to force a positive OD, such as those described by Van Houtte (1991), do not have an effect in this case as the even coefficients are the only ones that are used in preferred-orientation correction and are not affected by positivity or similar methods. Constraints to force positive texture-correction factors are already provided by the experimental pattern. Additional constraints may be added to force the OD to also have positive texture factors or to remain inside the measured bounds.

An alternative approach is to write the OD as $f(g) = \exp[h(g)]$ (in a similar fashion to the exponential-harmonic method of Van Houtte, 1991) and to expand the function $h(g)$ in terms of spherical harmonics. This will retain all of the symmetries of the OD and ensure an OD that is always positive. The problem is that the texture factors can no longer be calculated using (5.3.13) and should be evaluated by numerical integration over the OD using (5.3.11), and in the Rietveld least-squares method only the numerical derivative must be adopted.

5.3.4.6. The use of standard functions (or texture components)

An alternative model for preferred orientation is to use standard components. In the case of only one pattern, fibre components should be used or fibre sample symmetry as described in Section 5.3.2.3.7. To compute a pole-figure value or texture model for a general fibre component having a partial Gaussian and Lorentzian character, (5.3.29) and (5.3.31) can be used by integrating around the fibre axis.

5.3.4.7. Remarks

In most of the previous models, the formulations are only valid for axially distributed, single-component textures (with a cylindrical symmetry around the scattering vector, and for a Bragg–Brentano symmetric geometry), for which efficient corrections are obtained (O'Connor *et al.*, 1991; Capková *et al.*,

Table 5.3.1
Preferred-orientation (PO) modelling methods implemented in some Rietveld packages, and their capability to perform a full texture analysis (QTA) with determination of the OD from several patterns

Details are given in the form yes/no for PO correction/full QTA (OD refinement).

Software	GSAS	FullProf	TOPAS	MAUD	Jana	BGMN	RIETAN	WinMprof
March–Dollase	Yes/no	Yes/no	Yes/no	Yes/no	Yes/no	Yes/no	Yes/no	Yes/no
Donnet–Jouanneaux	No/no	No/no	No/no	No/no	No/no	No/no	No/no	Yes/no
Spherical harmonics	Yes/yes	No/no	No/no	Yes/yes	No/no	No/no	No/no	No/no
Exponential harmonic	No/no	No/no	No/no	Yes/yes	No/no	†/no	No/no	No/no
WIMV	No/no	No/no	No/no	Yes/yes	No/no	No/no	No/no	No/no
EWIMV	No/no	No/no	No/no	Yes/yes	No/no	No/no	No/no	No/no
Standard components	No/no	No/no	No/no	Yes/yes	No/no	No/no	No/no	No/no

† In this case an exponential-harmonics method is claimed, but the particular implementation does not ensure compatibility between pole-figure and OD values.

1993; Cerný *et al.*, 1995). They have been implemented in many Rietveld programs, and some of them allow the modelling of two or more texture components of this type. For all other textures, measurements and formalisms to resolve the texture are required, unless the conversion of the sample to powder is acceptable. Furthermore, one should take particular care regarding the geometry used for the measurements. The previous formulae describe the orientations in the sample reference frame, while measurements are carried out in the spectrometer frame. The relationships between the two frames are straightforward when using classical θ–2θ scans, but for any other measurements, such as rocking curves or the use of area detectors, for instance, prior localization corrections have to be made to locate the plane normals in the sample frame.

The previous models do not allow the description of texture either in terms of orientations or of distribution densities (expressed in m.r.d. units), based on the absence of OD calculations implying normalization. Also, many Rietveld-based programs offer preferred-orientation modelling capabilities, but do not always include OD refinement, *i.e.* not reaching the QTA stage (Table 5.3.1).

In particular, working on whole patterns became mandatory with the growing demand for the characterization of nanocrystalline samples. In such samples, the tremendous inter-phase and intra-phase overlaps prevent any correct QTA characterization if proper deconvolutions are not carried out. A Rietveld-like approach becomes mandatory, with the advantage of then being able to access other material characteristics such as residual stresses, phase amounts and line broadening. This is the subject of combined analysis.

5.3.5. Combined analysis: structure, texture, microstructure, stress, phase, layering and reflectivity analyses in a single approach

5.3.5.1. *Problems*

Analysis by the diffraction/scattering of X-rays is presently facing a major problem: the nondestructive characterization of samples with increasing complexity (thin or massive heterostructures, polyphase materials, hybrids *etc.*), including as many as possible of their characteristics (structure, texture, crystallite sizes). These real samples often exhibit optimized properties because of their anisotropy, and this creates some problems in data analysis.

Problem 1. Anisotropic samples exhibit diffraction diagrams depending on the sample orientation because of the presence of texture. Refinement of crystal structures requires a model for the texture, as shown in Section 5.3.4. Texture factors depend on sample orientation, whereas structure factors do not. Also,

texture factors integrate to unity over the entire pole figure. This indicates that with a proper approach to the problem (exploiting the full texture analysis), texture and structure are completely uncorrelated and can easily be decoupled. Full (and sharp) texture can actually be used as an advantage in structure solution (Wessels *et al.*, 1999).

Problem 2. Anisotropy is induced during production (*e.g.* heteroepitaxy, uniaxial pressing *etc.*), along with residual stresses in the sample. The diffraction peaks are then shifted relative to their unstressed positions, which biases on the one hand structural determination (unit-cell parameters) and on the other hand QTA, since the peak positions vary with the necessary rotations of the sample for texture measurements. It is then necessary to analyse the residual stresses in order to determine both the structure and texture correctly. However, differently oriented crystallites do not deform identically under the same macroscopic stress thanks to their tensorial elastic properties (anisotropic if texture is present), and a mutual influence exists between texture and residual stresses. Thus, there is a need to analyse both texture and stress simultaneously to obtain more accurate values of each.

Problem 3. Samples can be composed of several layers of different phases, which then have to be characterized individually in terms of structure/texture/stress. Volume and absorption variations are not the same for a covered layer, a top film or a substrate, and have an effect on intensities measured at different 2θ and **y** positions. These variations, if unaccounted for, bias structural, quantitative and textural analyses. The corrections to be applied depend on the effective thicknesses of the layers and their absorption coefficients, and thus depend on the phase composition.

Problem 4. In polyphase materials (completely or partially crystalline), quantitative phase analysis (QPA) can be biased if texture is present, and a suitable model is necessary in the analysis. Simple models such as the March–Dollase model should be avoided. The texture should be fully accounted for or removed by suitable sample preparation.

Problem 5. All of these results (structure, QTA, QPA, residual stress analysis and layering) depend on the microstructural states, crystallite sizes and shapes (isotropic or anisotropic), crystalline defects (point, linear, planar or volumetric), composition variations and microstrains, which in turn will be correctly determined only if the other parameters are satisfactorily known. Let us take the example that crystallite size effects are revealed in the line broadening and are then decoupled from (for instance) texture, which induces only intensity variations. This working hypothesis is, however, only valid if no peak overlap occurs. Indeed, if overlap is present the separation of each individual line broadening will depend on the convoluted intensities, which in turn depend on the texture (and/or other intensity effects). In a multi-

component line, it will become dangerous to separate the components without somehow constraining the intensities, which can be performed using both $F_{\mathbf{h}}$ and $f(g)$ information. Conversely, the correct estimation of each intensity for subsequent QTA requires the separation step, implying some knowledge of the broadening.

Problem 6. All of the previous determinations rely on an *a priori* knowledge of the exact material composition to be characterized. Unfortunately, compositions may vary from sample to sample, giving rise to incorrect assignments of parameters during refinement. For instance, we may have the same atoms distributed over multiple phases in an unknown way, or multiple atoms occupying the same crystallographic site in one or more phases. In such a case one needs to constrain the problem, using for instance elemental compositions from energy-dispersive X-ray spectroscopy (EDX) or X-ray fluorescence (XRF). Also, for a quantitative XRF or EDX analysis a precise knowledge of the phase concentrations is fundamental to estimate the matrix effect or absorption. Chemical analysis by EDX or XRF may benefit from a quantitative analysis by diffraction, as well as the reverse. Thus, there is a need for a combined analysis, either based on independent *in situ* or *ex situ* measurements of the same samples.

The question arises after this list of problems as to whether one could benefit from the anisotropy of the material, and/or from the multiple independent measurements necessary to carry out a complete characterization of the real material. Such an approach needs to take account of all the effects visible in the diffracted signal, to measure a sufficient number of independent data with different techniques when necessary, and perform a single fitting of the full data by either least-squares or other suitable methods.

5.3.5.2. *Intensity of a pattern and general scheme*

If we consider a sample composed of N_L layers (a bulk sample is then equivalent to a single layer of infinite thickness) and N_Φ phases distributed in the layers, the intensity of a single data point $\mathbf{y}_c$ at 2θ and η (see Section 5.3.2.1.3.3 for angle definitions) in a diffractogram measured at a given sample orientation $\mathbf{y}_S$ ($\mathbf{y}_S$ represents the sample orientation in the spectrometer space S, *i.e.* defined by the goniometer angles ω, χ and φ) can be calculated as the sum of all reflections contributing to that point for all phases in all layers,

$$
\begin{aligned}
y_c(\mathbf{y}_S, \theta, \eta) = {} & y_b(\mathbf{y}_S, \theta, \eta) \\
& + I_0 \sum_{i=1}^{N_L} \sum_{\Phi=1}^{N_\Phi} \frac{v_{i\Phi}}{V_{c\Phi}^2} \sum_{\mathbf{h}} \mathrm{Lp}(\theta) j_{\Phi\mathbf{h}} |F_{\Phi\mathbf{h}}|^2 \Omega_{\Phi\mathbf{h}}(\mathbf{y}_S, \theta, \eta) \\
& \times P_{\Phi\mathbf{h}}(\mathbf{y}_S, \theta, \eta) A_{i\Phi}(\mathbf{y}_S, \theta, \eta),
\end{aligned}
$$

$$(5.3.63)$$

in which y_b is the background contribution, I_0 is the incident intensity on the sample, $v_{i\Phi}$ is the volumetric fraction of phase Φ in layer i, $V_{c\Phi}$ is the unit-cell volume of phase Φ, Lp is the Lorentz polarization factor, $j_{\Phi\mathbf{h}}$ is the multiplicity of line $\mathbf{h}$ for phase Φ, $|F_{\Phi\mathbf{h}}|$ is the modulus of the structure factor (including thermal vibrations) for line $\mathbf{h}$ of phase Φ, $\Omega_{i\Phi\mathbf{h}}$ is the profile function of line $\mathbf{h}$ for phase Φ, taking account of instrumental and sample broadenings, $P_{\Phi\mathbf{h}}$ is the preferred orientation (pole-figure value) of phase Φ and $A_{i\Phi}$ is an absorption factor which takes into account the experimental and sample geometries.

In a similar way, we can write the intensity of a measured point in a pattern for reflectivity and XRF or EDX. We will explicitly write the equations for the diffraction part, but the procedure can be extended to every technique for which a measured intensity

can be written in terms of the parameters describing the sample. The overall weighted sum of squares, as in Rietveld joint refinements, can then be written as a weighted sum between different techniques, each measuring a certain number of patterns and with each pattern t composed of N_t measured points:

$$
\mathrm{WSS} = \sum_{t=1}^{N_p} u_t \sum_{i=0}^{N_t} w_{it}(y_{itc} - y_{ito})^2. \tag{5.3.64}
$$

The weight w_{it} is usually related to the inverse of the measured intensity for point i of pattern t and is equal to the inverse of the square of the standard deviation. Each pattern t is weighted using the quantity u_t, which should be used to adjust the importance that we want to give to a particular technique or pattern with respect to the others.

The quantity WSS must be minimized to find the optimized parameters. The minimization can be performed through standard nonlinear least-squares methods or other minimization schemes depending on the particular models that are used and the efficiency of the algorithm for a given problem.

5.3.5.3. *Minimum experimental requirements*

This methodology requires a large amount of data, however, and to be practical requires rapid acquisition using, for example, multiple detectors. The first experiment using such an approach was carried out with X-rays on a thin film (Ferrari & Lutterotti, 1994) on a laboratory texture instrument using a scintillator detector. The first experiment of this kind using neutron TOF data (Lutterotti *et al.*, 1997) was performed on the General Purpose Powder Diffractometer (GPPD) at the Intense Pulsed Neutron Source (IPNS). Since then, the methodology has been used for various purposes (Chateigner *et al.*, 1998; Lutterotti *et al.*, 2002, 2004; Morales *et al.*, 2002, 2005; Ricote *et al.*, 2004; Guilmeau *et al.*, 2005).

The required diffractometer has to be equipped with four circles in order to correspond to a texture experiment, *i.e.* at least one tilt rotation χ, one azimuthal rotation φ, an incidence circle ω and a detection circle 2θ. One circle (one scanning movement) can be eliminated by using a linear detector on the 2θ arm. Another circle and scan can be saved by using bidimensional detectors.

5.3.5.4. *Theoretical implementation*

5.3.5.4.1. *Instrumental broadening calibration*

The spectrometer space is multidimensional, with each rotation axis possibly giving rise to defocusing or misalignment effects. Each of these aberrations has to be measured and corrected for. For instance, in dealing with goniometer misalignments (which should be minimized as much as possible by careful alignment of the instrument and the sample) one can model them to a certain extent in the computation by reproducing all effects of sample displacements, precession errors and angle offsets. The fitting of instrument- and sample-misalignment errors should only be used as a last resort, and a well performed experiment is obviously always preferred. Fig. 5.3.19 is an illustration of such aberrations measured on a KCl standard powder using a four-circle diffractometer and a curved position-sensitive detector (CPS 120 from Inel).

Three major effects are visible: peak broadening, peak shift and background variation.

Broadening occurs when the incident beam illuminates the sample surface, producing variations in the irradiated area and the apparent Bragg-angle values. These were originally called
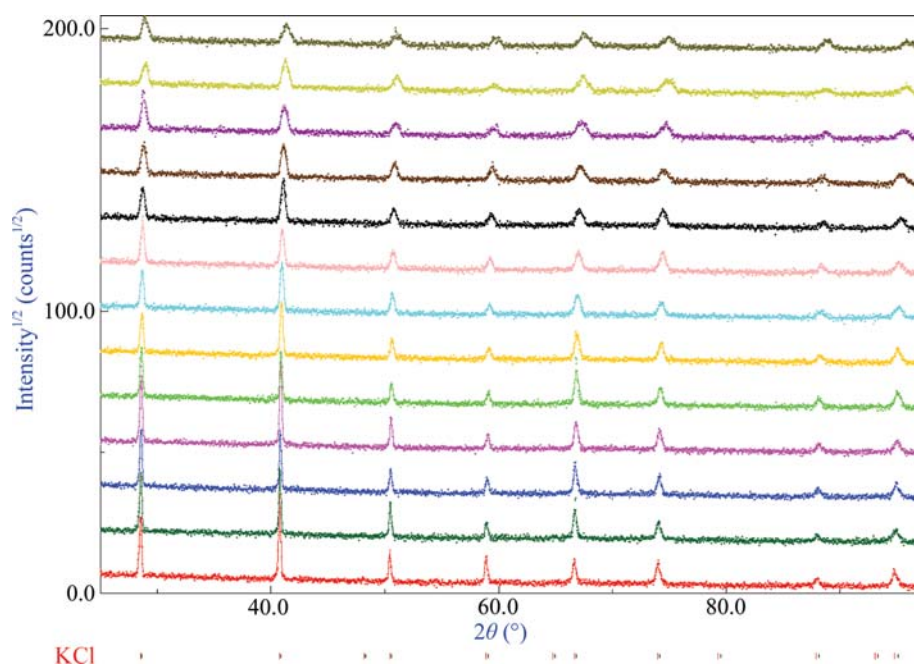
Figure 5.3.19
Illustration of the effects of defocusing and misadjustment on peak shapes and diffractometer resolution function. Measurements are on KCl powder. Diffractograms appear on top of each other from $\chi = 0°$ to $\chi = 60°$ in steps of $5°$ and were measured for $\omega = 20°$.

'defocusing effects', even if the experimental setup does not properly incorporate focusing optics (as in this case with the use of a parallel beam). They are dependent on the various angles of sample rotation.

When the sample tilt χ increases, the peaks broaden. For a square incident-beam cross section, the irradiated area on the flat sample is a rectangle at $\chi = 0°$ and becomes a parallelogram at $\chi > 0°$. The beam-footprint size then increases, giving rise to apparent θs and broadened peaks. For a bulk sample in symmetric reflection geometry the total integrated intensity remains constant whatever the value of χ (Schulz, 1949a). This implies that when using the full profile the defocusing effect is automatically taken into account since the total integrated area of the pattern is unchanged. However, at values of χ that are too large (typically >60°) the peak maxima decrease to values that are closer to the background, and even the integrated intensities are less reliable because of poorer counting statistics. This obviously depends on the instrumental setup, such as the detecting slit aperture, and can be partly compensated for by using larger counting times at larger χ values, but this always remains a compromise. For instance, increasing the detecting slit can provide a lower defocusing effect because of a larger integrating window, but as a result enhances the instrumental broadening and peak overlaps, and can prevent any microstructural analysis.

For a given diagram measured at ω, the peaks are broader at larger 2θ (Fig. 5.3.20). This effect is typical of flat specimen analyses; it does not occur, for instance, in transmission geometry using neutrons. For a given peak at 2θ, the full width at half maximum (FWHM) is smaller at larger ω angles owing to the smaller irradiated area of the sample. This effect also is typical of flat specimen analyses in reflection geometry and using a parallel beam.

In order to analyse the line broadening due to the characteristics of the sample, all of the various instrumental broadenings either have to be known from measuring the instrumental profiles using a standard sample with a known sample broadening or must

be computed. The latter still requires the measurement of certain characteristics such as the tube focus.

A polynomial-like equation can then be used to represent the variations in the squared FWHM of the lines with the angles in a similar fashion to the Caglioti formula (Caglioti *et al.*, 1958),

$$\Delta_r\mathrm{FWHM}^2 = \sum_{u=0}^{U} p_{ru}r^u, \qquad (5.3.65)$$

with r as a general rotation (χ, θ, $\tan\theta$, ω, η, ...) and with as many p_{ru} parameters as necessary, introducing them progressively in the refinement until they refine to negligible values.

5.3.5.4.2. *Peak-displacement errors*

Peak shifts arise from the misalignment of one or several of the rotation axes or sample displacement from the rotation centre. For instance, in Fig. 5.3.20 we clearly observe a 2θ peak shift for large χ values and this shift would not be the same at two different ω values. Depending on the experimental configuration, analytical formulae can be produced to fit these misalignments. If information about unit-cell parameters and/or residual strain are important, it is advisable to either have a perfectly aligned system or to use analytical formulae based on the geometrical features of the misalignment. Other empirical corrections are possible, based on polynomial fits or parametrizations per pattern, that are efficient for the correction of the peak position, but are more likely to cause a loss of positional information. These corrections are instrument dependent.

5.3.5.4.3. *Background fitting*

Furthermore, depending on many factors such as sample shape and absorption, the background B can also vary with the various angles of rotation. These variations have to be modelled, which is usually accomplished through a polynomial fit on all rotation axes,

$$\Delta_r B = \sum_{u=0}^{U} p'_{ru}r^u \qquad (5.3.66)$$

or more complex functions such as Chebyshev polynomials (Larson & Von Dreele, 2000; Press *et al.*, 1988),

$$\Delta_r B = \sum_{u=0}^{U} p''_{ru} T_u(r^*), \quad r^* = \frac{2(r - r_{\min})}{r_{\max} - r_{\min}} - 1, \qquad (5.3.67)$$

where p'_{ru} and p''_{ru} are the factors to be determined. For Chebyshev polynomials the value of r must be substituted with r^* to be orthonormal, and $r_{\min}$ and $r_{\max}$ define the range of r.

Another option is to use an interpolated background which, instead of being applied to the original pattern (not advisable in Rietveld-like fitting), is applied to the residual pattern (the experimental data minus the computed profile) as in *MAUD* (Lutterotti, 2010). In this manner, the interpolation will not take intensity from the reflections as long as these are properly fitted.

In QTA with point detectors background subtraction is never easy; the evolution of background with rotation axes is not easily measured (because of defocusing from nearby peaks, for
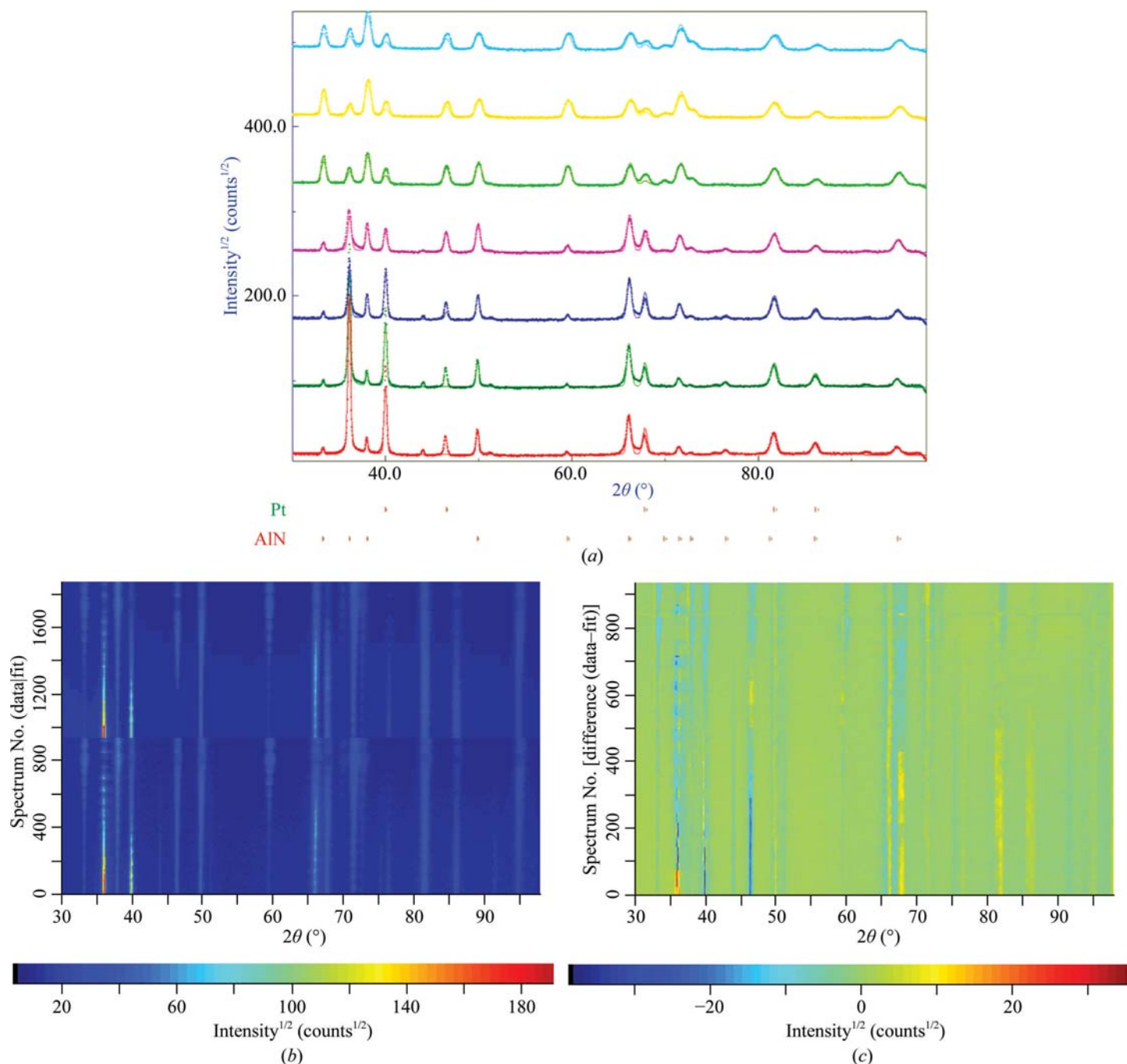
Figure 5.3.20
(*a*) Randomly selected diagrams (at increasing χ values and broadening due to defocusing from bottom to top) illustrating the quality of the fit, together with the textures of AlN and Pt. (*b*) Two-dimensional plots of the 936 experimental (lower half) and fitted (upper half) diagrams and (*c*) two-dimensional difference diagrams to reveal the errors.

instance) and is sample dependent. Here, one can see another advantage of full-profile analysis, where the background is not removed *a priori* but is modelled along with the reflection intensities.

5.3.5.4.4. *Reflection intensities*

Reflection intensities, as appearing in (5.3.63), depend mainly on the structure factors described elsewhere in this volume. Three different approaches are used to calculate them in the combined-analysis scheme.

The first approach calculates the structure factors from the atomic model with knowledge of the types and positions of the atoms in the unit cell. If an accurate crystal structure is not available for a particular phase, some information loss occurs

(mainly phase concentrations and layer information), but we can still understand several other characteristics if at least an indexing of the phase is available. For most of the other properties (texture, stresses, anisotropic crystallite sizes and microstrains *etc.*) only the Laue group and an initial estimation of the unit-cell parameters are required. In this case, we can use the other two approaches.

The second approach starts from knowledge of the Laue group (or, better, the space group if available) and uses Le Bail or Pawley refinement for the intensities. In the case of Pawley refinement all of the reflection intensities become parameters to be refined (this is exactly equivalent to a whole-pattern fitting), and the exactly overlapped parameters should be treated as summed to achieve convergence. Normally this approach is rapid when the phase has a small number of reflections, but it becomes

very difficult to carry out a fit when this number is very large. In this latter case the Le Bail approach is more efficient, and one can always switch to Pawley refinement just for the last iterations when the fitting is already satisfactory. These two methods are discussed in Chapter 3.5.

The third approach is a variant of the second, using an electron-density map (or a nuclear-density map for neutron diffraction) obtained from the extracted structure factors (using either one of the two methods mentioned above) at each iteration to calculate the intensities to be used in the fitting. This will force the structural intensities to be compatible with an electron-density map, providing a strong constraint for the severely overlapped peaks. It is assumed that by iteration the problem will converge toward the real electron-density map, but this cannot be ensured.

When associated with a strong texture of the sample, the second and third approaches can be used to obtain single-crystal-like structure factors that can be used to obtain the structure, as described by Wessels *et al.* (1999) and in a more recent variant in which texture and structure factors are extracted simultaneously from the same data (Lutterotti & Bortolotti, 2005; Grässlin *et al.*, 2015).

5.3.5.4.5. *Line profiles and sample broadening*

Profile functions are described as a convolution of two terms: the instrumental broadening and the sample broadening. In the combined approach we utilize the two explicitly separated contributions to perform refinement directly using the micro-structural characteristics as parameters (Lutterotti & Scardi, 1990; Lutterotti & Gialanella, 1998; Lutterotti, 2010). If the instrumental broadening is known (see Section 5.3.5.4.1) we only need to refine the parameters concerning the sample broadening, and the best approach to ensure better convergence and more reliable results is to describe the sample broadening using physical quantities.

With respect to line-broadening theories, we note here that for this method we need equations and methods that allow computation of the sample-broadening profile from the microstructural characteristics and not the reverse.

These methods can be divided into two categories. The first category contains methods that describe the sample broadening using analytical functions, for which theory describes the variation of the parameters as a function of the scattering unit caused by the microstructural characteristics (Lutterotti & Scardi, 1990; Lutterotti & Gialanella, 1998). The second category does not impose analytical functions on the profile, but instead computes the profile directly from the crystallite size and microstrain distributions using the interference function (Lutterotti & Scardi, 1992), the Fourier transform (Ungár *et al.*, 2001; Lutterotti, 2010) or analytical approximations (Popa & Balzar, 2002). In the latter case it is the analytical shape of the distribution that is imposed. The crystallite and microstrain anisotropies, which cause anisotropy of the reflection broadenings, have been described previously by empirical formulae (Lutterotti & Scardi, 1990) or by taking into account the crystallographic symmetry restrictions (Popa, 1998), and can be coupled with the distribution-calculation method (Popa & Balzar, 2008).

In addition to crystallite sizes and microstrains, other microstructural characteristics have been included in the combined analysis as planar defects following Warren theory (Warren, 1969; Lutterotti & Gialanella, 1998) or turbostratic disorders (Ufer *et*

al., 2004; Lutterotti *et al.*, 2010); these are useful in the case of clay or graphitic materials.

5.3.5.4.6. *Texture computation*

The texture factors in (5.3.63) can be computed using one of the methods reported in Section 5.3.4 for Rietveld analysis, but only those associated with an OD computation, *i.e.* all but the empirical methods such as the March–Dollase and Donnet–Jouanneaux methods.

To ensure a physically meaningful texture analysis, two kinds of approach can be used in the combined analysis. The first is applicable when the pole figures can be computed through analytical functions containing the parameters to be refined. This is the case for the harmonic, exponential-harmonic and standard-components methods in Section 5.3.4. The implementation and the use of such methodologies is quite straightforward in the Rietveld framework.

A different case is the second approach (WIMV/EWIMV), in which there is no analytical function either to describe the OD or to compute the pole-figure values. This is performed through numerical integration using a discrete function with a very large number of unknowns. Therefore, by analogy to the electron-density case with structure factors, the method is to extract the texture values from patterns and use them to compute the OD, from which we can compute the texture value for the next Rietveld-like iteration step.

The extraction of the texture value (the difference between the random value and the measured value) can be performed using a modified Le Bail algorithm (Matthies *et al.*, 1997) working on the texture values instead of the structure factors. The resulting 'experimental' pole-figure values are used by the WIMV or EWIMV algorithms to compute the OD. After this, a final fitting of the patterns is performed using the quantities calculated from the OD as the texture values. In the case of WIMV an additional step is required before computing the OD, as WIMV requires the pole-figure data in a regular grid over the pole figures, and a cubic interpolation is used for this. On the other hand, EWIMV does not require such regular grids.

Much care is mandatory in using all of these methods in order to ensure that the measured data are sufficient to experimentally cover the entire OD. This can easily be checked using discrete methods such as WIMV/EWIMV, but not with others that may apparently work (output an OD) without having full coverage and thus with values for the uncovered part that depend on the assumptions made (for example, intrinsically when assuming an inappropriate specific texture symmetry as in the March–Dollase method or extrinsically when the unmeasured parts would have contained most of the texture information).

5.3.5.4.7. *Residual strains/stresses and evaluation of macroscopic tensors*

In the presence of residual stresses, diagrams measured at several tilt angles exhibit peak shifts that cannot be reproduced without correct modelling of the sample residual strains. These come from the macrostresses and microstresses in the sample and also depend on the crystallite orientations (ODs). There are two different methods to approach this problem in combined analysis. One makes use of elasticity theories and models the strains and thus the reflection shifts from the stresses; the other instead directly models the strains without any assumption about the relationship between strains and stresses.

In the first approach, defining $K_L = (X_L, Y_L, Z_L)$, a laboratory frame in which Z_L is coincident with the scattering vector, X_L lies in the plane defined by the incident and diffracted beams and is directed towards the detector, and $Y_L = (Z_L \times X_L)$, the deformation of the diffracting plane (direction 33 for the deformation tensor in K_L) is then

$$\bar{\varepsilon}_{33}^L(\bar{\sigma}; \mathbf{h}, \mathbf{y}) = \frac{1}{4\pi \tilde{P}_{\mathbf{h}}(\mathbf{y})} \left[\int_{\mathbf{h}\|\mathbf{y}} \varepsilon_{33}^L(\sigma; g) f(g) \, d\tilde{\varphi} + \int_{-\mathbf{h}\|\mathbf{y}} \varepsilon_{33}^L(\sigma; g) f(g) \, d\tilde{\varphi} \right]$$

$$\equiv S_{33kl}^L(\mathbf{h}, \mathbf{y}) \bar{\sigma}_{kl}^L. \qquad (5.3.68)$$

The crystallographic strain $\varepsilon_{33}^L(\sigma; g)$ depends on the macrostresses through the stress factor $S_{33kl}^L(\mathbf{h}, \mathbf{y})$ (Behnken & Hauk, 1991), and several schemes have been proposed to calculate it in the presence of texture using different averages over orientations as a theoretical basis. The most used are the Voigt (1928), Reuss (1929) and Hill (1952) models. In the Voigt case the stress factor does not depend on $\mathbf{h}$ and it imposes a linear behaviour in $\sin^2\psi$, whereas in the Reuss case it does not. The Voigt and Reuss models define upper and lower bounds, respectively, for the macrostresses, the macroscopic elastic constants (those of the real sample) and their average, but do not ensure the consistency of elastic properties (simultaneous stress and strain equilibria). Such consistency for elastic properties requires that the homogenized sample stiffness, $\langle C \rangle$, should be equal to the inverse of the homogenized compliance, $\langle S \rangle^{-1}$. Neither of the methods mentioned above meet this criterion. On the contrary, the geometric-mean approach guarantees such consistency.

Considering an ensemble of N grains, with each grain m having a volume fraction v_m and with S_m being the single-crystal compliance tensor of the grain rotated in the sample reference frame, the arithmetic mean is then

$$\langle S \rangle_a^{-1} = \left[\sum_{m=1}^N v_m S_m \right]^{-1} \neq \sum_{m=1}^N v_m S_m^{-1} = \langle S^{-1} \rangle_a = \langle C \rangle_{\text{geo}}, \quad (5.3.69)$$

where the left-hand and right-hand sides correspond to the arithmetic averaging in the Reuss and Voigt hypotheses, respectively. Instead, for the geometric mean (Matthies & Humbert, 1993) the inversion property is guaranteed,

$$\langle S \rangle_{\text{geo}}^{-1} = \exp\left[-\sum_{m=1}^N v_m \ln S_m \right] = \exp\left[\sum_{m=1}^N v_m \ln S_m^{-1} \right]$$

$$= \langle S^{-1} \rangle_{\text{geo}} = \langle C \rangle_{\text{geo}}$$

or

$$\langle S \rangle_{\text{geo}}^{-1} = \left[\prod_{m=1}^N S_m^{v_m} \right]^{-1} = \prod_{m=1}^N S_m^{-v_m} = \prod_{m=1}^N (S_m^{-1})^{v_m}$$

$$= \langle S^{-1} \rangle_{\text{geo}} = \langle C \rangle_{\text{geo}}. \qquad (5.3.70)$$

Replacing the subscript m with the rotation g to bring the crystal tensor into the sample frame, using the explicit notation with four indices for the rank-4 compliance tensor and replacing the summation with the integral over H space, we obtain

$$\langle S_{ijkl} \rangle_a = \int_H S_{ijkl}^0(g) f(g) \, dg, \quad S_{ijkl}^0(g) = \sum_{m,n,p,q=1}^3 g_{mi} g_{nj} g_{pk} g_{ql} S_{mnpq},$$

$$\langle S_{ijkl} \rangle_{\text{geo}} = \langle (\ln S)_{ijkl} \rangle_a. \qquad (5.3.71)$$

This modelling gives good estimates of the macroscopic elastic properties (Matthies & Humbert, 1995) and does not result in large calculation times, *i.e.* it is suitable for implementation in the routine combined algorithm to calculate the strain tensor inside the crystallite from the macrostresses of the sample.

Using (5.3.68), we make the hypothesis that the strains are constant inside the sample (the Voigt hypothesis), the macro elastic tensor is computed using the arithmetic mean of the stiffness and everything reduces to the analogous $\sin^2\psi$ method. If we consider the stresses in the sample to be constant, the elastic tensor is computed through the Reuss hypothesis or the average of the compliance tensor.

We examine here the interesting case of the geometric mean, where neither the stresses nor the strains are constant throughout the sample but vary as a function of grain orientation. This is the inverse problem with respect to the homogenization technique [equations (5.3.70) and (5.3.71)]. This case has been solved by Matthies and co-workers (Matthies *et al.*, 2001; Matthies & Vinel, 1994) in a two-step process. Let us first obtain the solution by using the geometric mean (GEO) method to directly compute the so-called pathGEO approximation. Writing the stress factor using the Reuss hypothesis,

$$S_{33kl}^L(\mathbf{h}, \mathbf{y}) = {}^{\text{Reuss}} S_{33kl}^{L,p}$$

$$= \frac{1}{4\pi \tilde{P}_{\mathbf{h}}(\mathbf{y})} \left[\int_{\mathbf{h}\|\mathbf{y}} S_{33kl}^0(g) f(g) \, d\tilde{\varphi} + \int_{-\mathbf{h}\|\mathbf{y}} S_{33kl}^0(g) f(g) \, d\tilde{\varphi} \right];$$

$$(5.3.72)$$

in analogy, the pathGEO approximation gives

$$S_{33kl}^L(\mathbf{h}, \mathbf{y}) = {}^{\text{pathGEO}} S_{33kl}^{L,p}$$

$$= \exp\left\{ \frac{1}{4\pi \tilde{P}_{\mathbf{h}}(\mathbf{y})} \left[\int_{\mathbf{h}\|\mathbf{y}} S_{33kl}^0(g) f(g) \, d\tilde{\varphi} + \int_{-\mathbf{h}\|\mathbf{y}} S_{33kl}^0(g) f(g) \, d\tilde{\varphi} \right] \right\}.$$

$$(5.3.73)$$

In the latter equation, we neglect the interaction of the matrix surrounding the crystallites. Adding it to the formulation, we obtain the final Bulk-PathGEO (BPG) formulation (Matthies & Humbert, 1995; Matthies *et al.*, 2001),

$$S^{L,\text{BPG}} = \left[\left(\langle S \rangle_{\text{geo}}^L \, {}^{\text{pathGEO}} S^L \right)^{1/2} \right]^{\text{sym}}, \qquad (5.3.74)$$

and we are interested in the $S_{33kl}^{L,\text{BPG}}$ components of (5.3.68).

Another approach has been developed which does not consider the nature of the residual stresses and may be more appropriate in the case of plastic deformation or when pure elastic strains/stresses are not present. The method aims to use the Rietveld method to extract the crystallographic stresses in order to obtain the so-called stress orientation distribution function (SODF). Details can be found in Wang *et al.* (2000, 2003).

In combined analysis, a variant of this method is used that is more suitable for implementation in a Rietveld code. This variant (Popa & Balzar, 2001) considers that texture and stresses are always coupled by (5.3.68), and instead of using the SODF it defines a so-called WSODF (weighted-strain ODF) that is the product of the crystallographic OD and the SODF. This simplifies the formalism greatly and avoids the propagation of the errors present in the OD to the SODF (which is one of the problems of the original method). The WSODF (and similarly the SODF) is then expanded using spherical harmonics, and the right-hand side of (5.3.68) can be written in terms of harmonic coefficients to be refined. We refer the reader to the original paper for details of the symmetrization and implementation.

Table 5.3.2
Results obtained from combined analysis on an AlN/Pt/TiO$_x$/Al$_2$O$_3$/Ni(Co–Cr–Al–Y) stack

Standard deviations are given in parentheses for the last digit.

	AlN	Pt	Al$_2$O$_3$	Ni(Co–Cr–Al–Y)
Unit-cell parameters (Å)	$a = 3.11203$ (1), $c = 4.98252$ (1)	$a = 3.91198$ (1)	$a = 4.7562$ (6), $c = 12.875$ (3)	$a = 3.569377$ (5)
Effective layer (nm)	14270 (3)	1204 (3)	7790 (31)	∞
Isotropic mean crystallite size (Å)	2404 (8)	2173 (10)	150 (2)	7600 (1900)
Isotropic mean microstrain (r.m.s.)	0.001853 (2)	0.002410 (3)	0.008 (3)	0.00236 (3)
Biaxial macrostresses (MPa)	$\sigma_{11} = -1019$ (2), $\sigma_{22} = -845$ (2)	$\sigma_{11} = -196.5$ (8), $\sigma_{22} = -99.6$ (6)	Not fitted	$\sigma_{11} = -328$ (8), $\sigma_{22} = -411$ (9)
F^2 (m.r.d.^{2})	9.30	5.36	—	1.04
OD R factors (%)	$R_w = 4.09$, $R_b = 4.41$	$R_w = 33.25$, $R_b = 26.63$	—	$R_w = 49.15$, $R_b = 37.38$

5.3.5.4.8. *Absorption and layers*

Computation of the absorption is another important part of the approach, especially considering some samples that do not meet the requirements of standard computation (Bragg–Brentano: specimen completely intercepts the beam, homogeneity inside the volume, infinite thickness; Debye–Scherrer: cylindrical or spherical shape, sample inside the beam, light absorber). In the simple case of a thin film or multilayers we already have a heterogeneous sample and special treatment of the absorption correction is needed. Another case is an irregular shape or a strong absorber in Debye–Scherrer geometry.

For multilayers, a first implementation to correctly approach the problem in a Bragg–Brentano geometry (Lutterotti *et al.*, 1993) is aimed at phase analysis in the layers. For a more comprehensive absorption correction for a multilayer sample that includes all possible geometries and cases, Simek *et al.* (2006) developed a correction that depends only on the incident angle θ_i of the beam (with respect to the plane parallel to the layering and surface of the sample) and the exit angle θ_o,

$$A_{i\Phi} = \frac{\nu_{i\Phi} \sin\theta_i \sin\theta_o}{\overline{\mu}_i(\sin\theta_i + \sin\theta_o)}[1 - \exp(-\overline{\mu}_i\tau_i W)]\prod_{k<i}\exp(-\overline{\mu}_k\tau_k W),$$

$$W = \frac{1}{\sin\theta_i} + \frac{1}{\sin\theta_o}, \qquad (5.3.75)$$

where $\overline{\mu}_i = \sum_{\Phi=1}^{N_\Phi}\nu_{i\Phi}\mu_{i\Phi}$ is the average linear absorption coefficient for layer i, $\mu_{i\Phi}$ is the absorption coefficient of phase Φ in layer i and τ_i is the thickness of layer i.

In the Debye–Scherrer geometry with either a strong absorber or an irregular sample shape, special care should be taken with the absorption computation. A general procedure has been developed (Xie *et al.*, 2004; Volz *et al.*, 2006) that represents the sample shape using the same harmonic expansion formulae as for the anisotropic crystallites (Popa, 1998) and uses a discretized integration of the beam path through the sample volume or a simplified path through the centre only (for computational speed; however, the shape refined is no longer representative of the sample).

5.3.5.5. *Implementation*

The combined-analysis software should allow the possibility of using X-ray (classical, synchrotron, monochromatic or energy dispersive, all scanning strategies and geometries, zero-dimensional, one-dimensional, flat and curved two-dimensional detectors) as well as neutron (thermal and TOF) or even electron data. It should be able to incorporate all formalisms corresponding to residual stress analysis (RSA), X-ray specular reflectivity, qualitative microstructure analysis, structure, QPA *etc.* and index diagrams for phase identification in an automatic approach [such as using the Crystallography Open Database (Grazulis *et al.*, 2009) or the Powder Diffraction File (Fawcett *et al.*, 2017)]. If the RSA of textured materials is of interest it should also offer tensor homogenization, openly accessing single-crystal tensors (Pepponi *et al.*, 2012). All of these requirement are actually met in the *MAUD* software (Lutterotti, 2010).

5.3.5.6. *Examination of a solution*

Using single-pattern refinement, a simple examination of the modelled and measured diagrams can suffice to detect refinement problems or refinement quality. When several hundreds of patterns are refined, such a comparison is cumbersome or simply impossible. One possibility to rapidly check whether the chosen
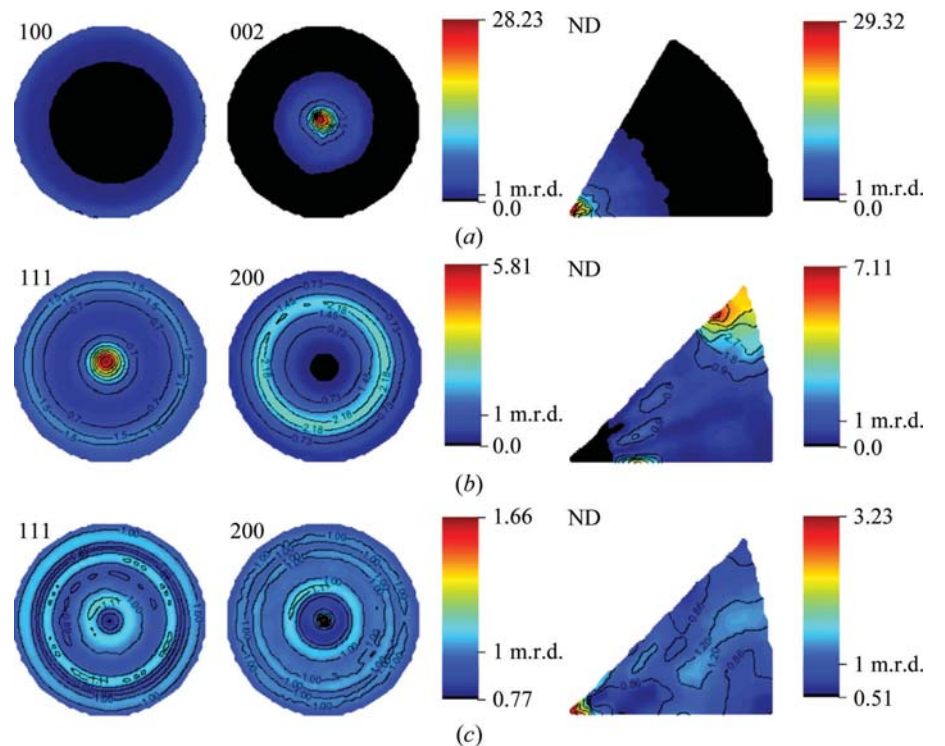

Figure 5.3.21
Low-index recalculated pole figures and Z_A inverse pole figures for the three textured phases of the stack. (*a*) AlN, (*b*) Pt, (*c*) Ni-based alloy. Equal-area density projections, linear density scale.

model is correct is to randomly select a small set of diffraction patterns to plot (Fig. 5.3.20*a*). However, such a method cannot prevent local strong discrepancies unless each diagram is examined in a laborious way. One can overcome this problem by plotting (for instance for an AlN/Pt/Al$_2$O$_3$/Ni alloy stack) all of the diagrams in a two-dimensional view (Fig. 5.3.20*b*), and completing the solution examination using two-dimensional residuals (Fig. 5.3.20*c*) in order to see where the main improvements to the model have to be carried out.

In such a case, combined analysis provides the characterization of the three ODs of Ni alloy, Pt and AlN, their respective biaxial residual stress states and structures. The layer thicknesses are also obtained with the crystallite isotropic sizes. The biaxial stress states are obtained using the geometric mean approach. All of the results are summarized in Table 5.3.2. These results were obtained within reliability factors of $R_w = 24.12\%$ and $R_{exp} = 5.85\%$ on 936 diagrams with a goodness of fit of 1.51.

The low-index pole figures of the three textured phases (Fig. 5.3.21) exhibit fibre textures with the fibre axis shifted slightly from the normal to the film plane Z_A. The substrate alloy shows the lowest texture strength; it is further increased in the Pt electrode and in the AlN film. This illustrates the electrical bias effect applied to the AlN orientation during sputtering, with a pronounced maximum of the {001} pole figure along Z_A of around 28 m.r.d. The Pt electrode exhibits a classical {111} orientation, with a slight tilt, while the Ni alloy is predominantly oriented with the {200} planes parallel to the sample plane. However, the corresponding inverse pole figures show that if AlN and Pt have a unique fibre orientation component, the Ni-alloy substrate also shows some minor fibre components.

The corresponding data for this example and many others can be found at http://www.ecole.ensicaen.fr/~chateign/formation/, together with some tutorials.

5.3.6. Conclusions

Classical quantitative texture analysis (and also residual stress, line broadening, phase composition *etc.*) becomes of questionable value for real samples that exhibit complex architectures with several phases and strong intra- and inter-phase peak overlapping. This is particularly true for poorly crystallized or nanocrystallized samples, for which line broadening is further enhanced. Proper deconvolution has to be carried out in such cases, which requires the use of full-pattern analysis in order to properly separate the various contributions to the diffraction diagrams (residual stresses, structure, phase content *etc.*). This can be elegantly achieved using the combined-analysis approach using X-rays, neutrons, electrons and *ad hoc* measurements.

References

Ahtee, M., Nurmela, M., Suortti, P. & Järvinen, M. (1989). *Correction for preferred orientation in Rietveld refinement. J. Appl. Cryst.* **22**, 261–268.

Behnken, H. & Hauk, V. (1991). *Berechnung der röntgenographischen Spannnungsfaktoren texturierter Werkstoffe – Vergleich mit experimentelle Ergebnissen. Z. Metallkde*, **82**, 151–158.

Birsan, M., Szpunar, A., Tun, Z. & Root, J. H. (1996). *Magnetic texture determination using nonpolarized neutron diffraction. Phys. Rev. B*, **53**, 6412–6417.

Brosnan, K. H., Messing, G. L., Meyer, R. J. Jr & Vaudin, M. D. (2006). *Texture measurements in ⟨001⟩ fiber-oriented PMN–PT. J. Am. Ceram. Soc.* **89**, 1965–1971.

Bunge, H.-J. (1969). *Mathematische Methoden der Texturanalyse*. Berlin: Akademie Verlag.

Bunge, H.-J. (1982). *Texture Analysis in Materials Science*. London: Butterworth–Heinemann.

Bunge, H.-J. & Esling, C. (1982). *Quantitative Texture Analysis*. Berlin: DGM Informationsgesellschaft Verlag.

Bunge, H.-J., Wenk, H.-R. & Pannetier, J. (1982). *Neutron diffraction texture analysis using a 2θ position sensitive detector. Textures Microstruct.* **5**, 153–170.

Caglioti, G., Paoletti, A. & Ricci, F. P. (1958). *Choice of collimators for a crystal spectrometer for neutron diffraction. Nucl. Instrum.* **3**, 223–228.

Capková, P., Peschar, R. & Schenk, H. (1993). *Partial multiplicity factors for texture correction of cubic structures in the disc-shaped crystallite model. J. Appl. Cryst.* **26**, 449–452.

Cerný, R., Valvoda, V. & Chládek, M. (1995). *Empirical texture corrections for asymmetric diffraction and inclined textures. J. Appl. Cryst.* **28**, 247–253.

Chateigner, D. (2005). *Reliability criteria in quantitative texture analysis with experimental and simulated orientation distributions. J. Appl. Cryst.* **38**, 603–611.

Chateigner, D. (2010). *Combined Analysis*. London/Hoboken: ISTE/Wiley.

Chateigner, D. & Erler, B. (1997). *Preferred orientations and epitaxial relationships of α-HgI$_2$ thin films on (001)-KCl and (001)-muscovite single crystals. Mater. Sci. Eng. B*, **45**, 152–161.

Chateigner, D., Germi, P. & Pernet, M. (1992). *Texture analysis by the Schulz reflection method: defocalization corrections for thin films. J. Appl. Cryst.* **25**, 766–769.

Chateigner, D., Germi, P. & Pernet, M. (1994*a*). *X-ray texture analysis of thin films by the reflection method: intermediate regime in defocusing corrections. J. Appl. Cryst.* **27**, 278–282.

Chateigner, D., Germi, P. & Pernet, M. (1994*b*). *X-ray texture analysis in films by the reflection method: principal aspects and applications. Mater. Sci. Forum*, **157–162**, 1379–1386.

Chateigner, D., Germi, P., Pernet, M., Fréchard, P. & Andrieu, S. (1995). *Fluorescence corrections in thin-film texture analysis. J. Appl. Cryst.* **28**, 369–374.

Chateigner, D., Hedegaard, C. & Wenk, H.-R. (2000). *Mollusc shell microstructures and crystallographic textures. J. Struct. Geol.* **22**, 1723–1735.

Chateigner, D., Lutterotti, L. & Hansen, T. (1998). *Quantitative phase and texture analysis on ceramics–matrix composites using Rietveld texture analysis. ILL Highlights*, **1997**, 28–29.

Chateigner, D., Ouladdiaf, B. & Léon, F. (2010). *Magnetic quantitative texture analysis using isotropic thermal neutron beams. Solid State Phenom.* **160**, 75–82.

Chernock, W. P. & Beck, P. A. (1952). *Analysis of certain errors in the X-ray reflection method for the quantitative determination of preferred orientations. J. Appl. Phys.* **23**, 341–345.

Coulomb, P. (1982). *Les Textures dans les Métaux de Réseaux Cubiques*. Paris: Dunod.

Couterne, J. C. & Cizeron, G. (1971). *Phénomène de défocalisation lié à la géométrie de la chambre de texture de Schulz et incidence sur l'intensité mesurée. J. Appl. Cryst.* **4**, 461–472.

Curien, H. (1971). *Les Groupes en Cristallographie*. In *Théorie des Groupes en Physique Classique et Quantique*, Vol. 2, edited by T. Kahan. Paris: Dunod.

Dahms, M. & Bunge, H.-J. (1988). *A positivity method for the determination of complete orientation distribution functions. Textures Microstruct.* **10**, 21–35.

Dollase, W. A. (1986). *Correction of intensities for preferred orientation in powder diffractometry: application of the March model. J. Appl. Cryst.* **19**, 267–272.

Durand, L., Kircher, F., Régnier, P., Chateigner, D., Pallerin, N., Gotor, F. J., Simon, P. & Odier, P. (1995). *Orientation of Y$_2$BaCuO$_5$ precipitates during unidirectional solidification of Y$_1$Ba$_2$Cu$_3$O$_{7-δ}$ under a magnetic field. Supercond. Sci. Technol.* **8**, 214–218.

Esling, C., Muller, J. & Bunge, H.-J. (1982). *An integral formula for the even part of the texture function or 'the apparition of the fn and fω ghost distributions'. J. Phys. (Paris)*, **43**, 189–196.

Fawcett, T. G., Kabekkodu, S. N., Blanton, J. R. & Blanton, T. N. (2017). *Chemical analysis by diffraction: the Powder Diffraction File. Powder Diffr.* **32**, 63–77.

Feng, C. (1965). *Determination of relative intensity in X-ray reflection study. J. Appl. Phys.* **36**, 3432–3435.

Ferrari, M. & Lutterotti, L. (1994). *Method for the simultaneous determination of anisotropic residual stresses and texture by X-ray diffraction. J. Appl. Phys.* **76**, 7246–7255.

Field, M. & Merchant, M. E. (1949). *Reflection method of determining preferred orientation on the Geiger-counter spectrometer. J. Appl. Phys.* **20**, 741–745.

Gale, B. & Griffiths, D. (1960). *Influence of instrumental aberrations on the Schultz technique for the measurement of pole figures. Br. J. Appl. Phys.* **11**, 96–102.

Grässlin, J., McCusker, L. B., Baerlocher, C., Gozzo, F., Schmitt, B. & Lutterotti, L. (2015). *Advances in exploiting preferred orientation in the structure analysis of polycrystalline materials. J. Appl. Cryst.* **46**, 173–180.

Grazulis, S., Chateigner, D., Downs, R. T., Yokochi, A. F. T., Quirós, M., Lutterotti, L., Manakova, E., Butkus, J., Moeck, P. & Le Bail, A. (2009). *Crystallography Open Database – an open-access collection of crystal structures. J. Appl. Cryst.* **42**, 726–729.

Gridi-Bennadji, F., Chateigner, D., Di Vita, G. & Blanchart, P. (2009). *Mechanical properties of textured ceramics from muscovite–kaolinite alternate layers. J. Eur. Ceram. Soc.* **29**, 2177–2184.

Guilmeau, E., Chateigner, D. & Noudem, J. G. (2003). *Effect of the precursor powders on the final properties of hot-forged Bi2223 textured discs. Supercond. Sci. Technol.* **16**, 484–491.

Guilmeau, E., Chateigner, D., Noudem, J., Funahashi, R., Horii, S. & Ouladdiaf, B. (2005). *Rietveld texture analysis of complex oxides: examples of polyphased Bi2223 superconducting and Co349 thermo-electric textured ceramics characterization using neutron and X-ray diffraction. J. Appl. Cryst.* **38**, 199–210.

Heidelbach, F., Riekel, C. & Wenk, H.-R. (1999). *Quantitative texture analysis of small domains with synchrotron radiation X-rays. J. Appl. Cryst.* **32**, 841–849.

Heizmann, J. J. & Laruelle, C. (1986). *Simultaneous measurement of several X-ray pole figures. J. Appl. Cryst.* **19**, 467–472.

Helming, K. (1992). *Minimal pole figure ranges for quantitative texture analysis. Texture Microstruct.* **19**, 45–54.

Hielscher, R. & Schaeben, H. (2008). *A novel pole figure inversion method: specification of the MTEX algorithm. J. Appl. Cryst.* **41**, 1024–1037.

Hielscher, R., Schaeben, H. & Chateigner, D. (2007). *On the entropy to texture index relationship in quantitative texture analysis. J. Appl. Cryst.* **40**, 371–375.

Hill, R. (1952). *The elastic behaviour of a crystalline aggregate. Proc. Phys. Soc. A*, **65**, 349–354.

Holland, J. R. (1964). *Quantitative determinations and descriptions of preferred orientation. Adv. X-ray Anal.* **7**, 86–93.

Huijser-Gerits, E. M. C. & Rieck, G. D. (1974). *Defocusing effects in the reflexion technique for the determination of preferred orientation. J. Appl. Cryst.* **7**, 286–290.

Imhof, J. (1982). *The resolution of orientation space with reference to pole figure resolution. Textures Microstruct.* **4**, 189–200.

Järvinen, M. (1993). *Application of symmetrized harmonics expansion to correction of the preferred orientation effect. J. Appl. Cryst.* **26**, 525–531.

Jouanneaux, A. (1999). *WinMPorf: a visual Rietveld software. International Union of Crystallography Commission on Powder Diffraction Newsletter*, **21**, 13.

Kocks, U. F., Kallend, J. S., Wenk, H.-R., Rollet, A. D. & Wright, S. I. (1994). *popLA: Preferred Orientation Package – Los Alamos*. Technical Report LA-CC-89-18, Los Alamos National Laboratory, USA.

Kocks, U. F., Tomé, C. N. & Wenk, H.-R. (1998). *Texture and Anisotropy*. Cambridge University Press.

Larson, A. C. & Von Dreele, R. B. (2000). *General Structure Analysis System (GSAS)*. Los Alamos National Laboratory Report LAUR 86-748.

Liu, Y. S., Depre, L., de Buyser, L., Wu, T. B. & van Houtte, P. (2003). *Intensity correction in texture measurement of polycrystalline thin films by X-ray diffraction. Textures Microstruct.* **35**, 283–290.

Lutterotti, L. (2010). *Total pattern fitting for the combined size–strain–stress–texture determination in thin film diffraction. Nucl. Instrum. Methods Phys. Res. B*, **268**, 334–340.

Lutterotti, L. & Bortolotti, M. (2005). *Algorithms for solving crystal structure using texture. Acta Cryst.* A**61**, c158–c159.

Lutterotti, L., Chateigner, D., Ferrari, S. & Ricote, J. (2004). *Texture, residual stress and structural analysis of thin films using a combined X-ray analysis. Thin Solid Films*, **450**, 34–41.

Lutterotti, L. & Gialanella, S. (1998). *X-ray diffraction characterization of heavily deformed metallic specimens. Acta Mater.* **46**, 101–110.

Lutterotti, L., Matthies, S., Chateigner, D., Ferrari, F. & Ricote, J. (2002). *Rietveld texture and stress analysis of thin films by X-ray diffraction. Mater. Sci. Forum*, **408–412**, 1603–1608.

Lutterotti, L., Matthies, S. & Wenk, H.-R. (1999). *MAUD – Materials Analysis Using Diffraction*. http://maud.radiographema.com/.

Lutterotti, L., Matthies, S., Wenk, H.-R., Schultz, A. J. & Richardson, J. W. (1997). *Combined texture and structure analysis of deformed limestone from time-of-flight neutron diffraction spectra. J. Appl. Phys.* **81**, 594–600.

Lutterotti, L. & Scardi, P. (1990). *Simultaneous structure and size-strain refinement by the Rietveld method. J. Appl. Cryst.* **23**, 246–252.

Lutterotti, L. & Scardi, P. (1992). *Profile fitting by the interference function. Adv. X-ray Anal.* **35**A, 577–584.

Lutterotti, L., Scardi, P. & Tomasi, A. (1993). *Application of the Rietveld method to phase analysis of multilayered systems. Mater. Sci. Forum*, **133–136**, 57–62.

Lutterotti, L., Voltolini, M., Wenk, H.-R., Bandyopadhyay, K. & Vanorio, T. (2010). *Texture analysis of a turbostratically disordered Ca-montmorillonite. Am. Mineral.* **95**, 98–103.

Manceau, A., Chateigner, D. & Gates, W. P. (1998). *Polarized EXAFS, distance-valence least-squares modeling (DVLS), and quantitative texture analysis approaches to the structural refinement of Garfield nontronite. Phys. Chem. Miner.* **25**, 347–365.

March, A. (1932). *Mathematische Theorie des Regelung nach der Korngestalt bei affiner Deformation. Z. Kristallogr.* **81**, 285–297.

Matthies, S. (1979). *On the reproducibility of the orientation distribution function of texture samples from pole figures (ghost phenomena). Phys. Status Solidi B*, **92**, K135–K138.

Matthies, S. (1980). *Standard functions in the texture analysis. Phys. Status Solidi B*, **101**, K111–K115.

Matthies, S. (1982). *Form effects in the description of the orientation distribution function (ODF) of texturized materials by model components. Phys. Status Solidi B*, **112**, 705–716.

Matthies, S., Helming, K., Steinkopff, T. & Kunze, K. (1988). *Standard distributions for the case of fibre textures. Phys. Status Solidi B*, **150**, K1–K5.

Matthies, S. & Humbert, M. (1993). *The realization of the concept of a geometric mean for calculating physical constants of polycrystalline materials. Phys. Status Solidi B*, **177**, K47–K50.

Matthies, S. & Humbert, M. (1995). *On the principle of a geometric mean of even-rank symmetric tensors for textured polycrystals. J. Appl. Cryst.* **28**, 254–266.

Matthies, S., Lutteroti, L. & Wenk, H.-R. (1997). *Advances in texture analysis from diffraction spectra. J. Appl. Cryst.* **30**, 31–42.

Matthies, S., Priesmeyer, H. G. & Daymond, M. R. (2001). *On the diffractive determination of single-crystal elastic constants using polycrystalline samples. J. Appl. Cryst.* **34**, 585–601.

Matthies, S. & Vinel, G. W. (1982). *On the reproduction of the orientation distribution function of texturized samples from reduced pole figures using the conception of a conditional ghost correction. Phys. Status Solidi B*, **112**, K111–K114.

Matthies, S. & Vinel, G. W. (1994). *On some methodical developments concerning calculations performed directly in the orientation space. Mater. Sci. Forum*, **157–162**, 1641–1646.

Matthies, S., Vinel, G. W. & Helming, K. (1987). *Standard Distributions in Texture Analysis*, Vol. 1, edited by K. Helming. Berlin: Akademie Verlag.

Matthies, S. & Wenk, H.-R. (2009). *Transformations for monoclinic crystal symmetry in texture analysis. J. Appl. Cryst.* **42**, 564–571.

Morales, M., Chateigner, D. & Fruchart, D. (2003). *Texture and magneto-crystalline anisotropy analysis of an oriented ErMn$_4$Fe$_8$C powder sample. J. Magn. Magn. Mater.* **257**, 258–269.

Morales, M., Chateigner, D., Lutterotti, L. & Ricote, J. (2002). *X-ray combined QTA using a CPS applied to a ferroelectric ultrastructure. Mater. Sci. Forum*, **408–412**, 113–118.

Morales, M., Leconte, Y., Rizk, R. & Chateigner, D. (2005). *Structural and microstructural characterization of nanocrystalline silicon thin films obtained by radio-frequency magnetron sputtering. J. Appl. Phys.* **97**, 034307.

O'Connor, B. H., Li, D. Y. & Sitepu, H. (1991). *Strategies for preferred orientation corrections in X-ray powder diffraction using line intensity ratios. Adv. X-ray Anal.* **34**, 409–415.

Pawlik, K. (1993). *Application of the ADC method for ODF approximation in cases of low crystal and sample symmetries. Mater. Sci. Forum*, **133–136**, 151–156.

Pawlik, K. & Ozga, P. (1999). *LaboTex: The Texture Analysis Software for Windows.* http://www.labosoft.com.pl/.

Pepponi, G., Gražulis, S. & Chateigner, D. (2012). *MPOD: a Material Property Open Database linked to structural information. Nucl. Instrum. Methods Phys. Res. B*, **284**, 10–14.

Popa, N. C. (1992). *Texture in Rietveld refinement. J. Appl. Cryst.* **25**, 611–616.

Popa, N. C. (1998). *The (hkl) dependence of diffraction-line broadening caused by strain and size for all Laue groups in Rietveld refinement. J. Appl. Cryst.* **31**, 176–180.

Popa, N. C. & Balzar, D. (2001). *Elastic strain and stress determination by Rietveld refinement: generalized treatment for textured polycrystals for all Laue classes. J. Appl. Cryst.* **34**, 187–195.

Popa, N. C. & Balzar, D. (2002). *An analytical approximation for a size-broadened profile given by the lognormal and gamma distributions. J. Appl. Cryst.* **35**, 338–346.

Popa, N. C. & Balzar, D. (2008). *Size-broadening anisotropy in whole powder pattern fitting. Application to zinc oxide and interpretation of the apparent crystallites in terms of physical models. J. Appl. Cryst.* **41**, 615–627.

Press, W. H., Teukolsky, S. A., Vetterling, W. T. & Flannery, B. P. (1988). *Numerical Recipes in C.* Cambridge University Press.

Radon, J. H. (1986). *On the determination of functions from their integral values along certain manifolds. IEEE Trans. Med. Imaging*, **5**, 170–176.

Reuss, A. (1929). *Account of the liquid limit of mixed crystals on the basis of the plasticity condition for single crystal. Z. Angew. Math. Mech.* **9**, 49–58.

Ricote, J. & Chateigner, D. (1999). *Quantitative texture analysis applied to the study of preferential orientations in ferroelectric thin films. Bol. Soc. Esp. Ceram. Vidrio*, **38**, 587–591.

Ricote, J., Chateigner, D., Morales, M., Calzada, M. L. & Wiemer, C. (2004). *Application of the X-ray combined analysis to the study of lead titanate based ferroelectric thin films. Thin Solid Films*, **450**, 128–133.

Rietveld, H. M. (1969). *A profile refinement method for nuclear and magnetic structures. J. Appl. Cryst.* **2**, 65–71.

Roe, R.-J. (1965). *Description of crystallite orientation in polycrystalline materials. III. General solution to pole figure inversion. J. Appl. Phys.* **36**, 2024–2031.

Ruer, D. (1976). *Méthode vectorielle d'analyse de la texture.* Thesis. Université de Metz, France.

Ruer, D. & Baro, R. (1977). *A new method for the determination of the texture of materials of cubic structure from incomplete reflection pole figures. Adv. X-ray Anal.* **20**, 187–200.

Schaeben, H. (1988). *Entropy optimization in quantitative texture analysis. J. Appl. Phys.* **64**, 2236–2237.

Schaeben, H. (1991*a*). *Entropy optimization in quantitative texture analysis. II. Application to pole-to-orientation density inversion. J. Appl. Phys.* **69**, 1320–1329.

Schaeben, H. (1991*b*). *Determination of complete ODF using the maximum entropy method.* In *Advances and Applications of Quantitative Texture Analysis*, edited by H.-J. Bunge & C. Esling, pp. 109–118. Oberursel: DGM Informationsgesellschaft Verlag.

Schaeben, H. & van den Boogaart, K. G. (2003). *Spherical harmonics in texture analysis. Tectonophysics*, **370**, 253–268.

Schulz, L. G. (1949*a*). *A direct method of determining preferred orientation of a flat reflection sample using a Geiger counter X-ray spectrometer. J. Appl. Phys.* **20**, 1030–1033.

Schulz, L. G. (1949*b*). *Determination of preferred orientation in flat transmission samples using a Geiger counter X-ray spectrometer. J. Appl. Phys.* **20**, 1033–1036.

Shannon, C. E. (1948). *A mathematical theory of communication. Bell Syst. Tech. J.* **27**, 379–423.

Simek, D., Kuzel, R. & Rafaja, D. (2006). *Reciprocal-space mapping for simultaneous determination of texture and stress in thin films. J. Appl. Cryst.* **39**, 487–501.

Tenckhoff, E. (1970). *Defocusing for the Schulz technique of determining preferred orientation. J. Appl. Phys.* **41**, 3944–3948.

Ufer, K., Roth, G., Kleeberg, R., Stanjek, H., Dohrmann, R. & Bergmann, J. (2004). *Description of X-ray powder pattern of turbostratically disordered layer structures with a Rietveld compatible approach. Z. Kristallogr.* **219**, 519–527.

Ungár, T., Gubicza, J., Ribárik, G. & Borbély, A. (2001). *Crystallite size distribution and dislocation structure determined by diffraction profile analysis: principles and practical application to cubic and hexagonal crystals. J. Appl. Cryst.* **34**, 298–310.

Vadon, A. (1981). *Généralisation et optimisation de la méthode vectorielle d'analyse de la texture.* Thesis. Université de Metz, France.

Van Houtte, P. (1983). *The use of a quadratic form for the determination of non-negative texture functions. Textures Microstruct.* **6**, 1–19.

Van Houtte, P. (1991). *A method for the generation of various ghost correction algorithms – the example of the positivity method and the exponential method. Textures Microstruct.* **13**, 199–212.

Voigt, W. (1928). *Lehrbuch der Kristallphysik.* Leipzig: Teubner Verlag.

Volz, H. M., Vogel, S. C., Necker, C. T., Roberts, J. A., Lawson, A. C., Williams, D. J., Daemen, L. L., Lutterotti, L. & Pehl, J. (2006). *Rietveld texture analysis by neutron diffraction of highly absorbing materials. Powder Diffr.* **21**, 114–117.

Von Dreele, R. B. (1997). *Quantitative texture analysis by Rietveld refinement. J. Appl. Cryst.* **30**, 517–525.

Wagner, F. & Dahms, M. (1991). *Determination of complete ODFs with an optimized positivity method.* In *Advances and Applications of Quantitative Texture Analysis*, edited by H.-J. Bunge & C. Esling, pp. 101–108. Oberursel: DGM Informationsgesellschaft Verlag.

Wang, Y. D., Peng, R. L., Zeng, X. H. & McGreevy, R. (2000). *Stress-orientation distribution function (SODF) – description, symmetry and determination. Mater. Sci. Forum*, **347–349**, 66–73.

Wang, Y. D., Wang, X.-L., Stoica, A. D., Richardson, J. W. & Peng, R. L. (2003). *Determination of the stress orientation distribution function using pulsed neutron sources. J. Appl. Cryst.* **36**, 14–22.

Warren, B. E. (1969). *X-ray Diffraction.* Reading: Addison-Wesley.

Wenk, H.-R. (1985). *Preferred Orientation in Deformed Metals and Rocks: An Introduction to Modern Texture Analysis.* New York: Academic Press

Wenk, H.-R., Bunge, H.-J., Kallend, J. S., Lücke, K., Matthies, S., Pospiech, J. & Van Houtte, P. (1988). *Orientation Distributions: Representation and Determination.* In *Proceedings of the Eighth International Conference on Textures of Materials*, edited by J. S. Kallend & G. Gottstein, pp. 17–30. Warrendale: The Metallurgical Society.

Wenk, H.-R., Chateigner, D., Pernet, M., Bingert, J., Hellstrom, E. & Ouladdiaf, B. (1996). *Texture analysis of Bi-2212 and 2223 tapes and wires by neutron diffraction. Physica C*, **272**, 1–12.

Wenk, H.-R., Matthies, S., Donovan, J. & Chateigner, D. (1998). *BEARTEX: a Windows-based program system for quantitative texture analysis. J. Appl. Cryst.* **31**, 262–269.

Wessels, T., Baerlocher, C. & McCusker, L. B. (1999). *Single-crystal-like diffraction data from polycrystalline materials. Science*, **284**, 477–479.

Williams, R. O. (1968). *Analytical methods for representing complex textures by biaxial pole figures. J. Appl. Phys.* **39**, 4329–4335.

Xie, Y., Lutterotti, L. & Wenk, H.-R. (2004). *Texture analysis of ancient coins with TOF neutron diffraction. J. Mater. Sci.* **39**, 3329–3337.

Zolotoyabko, E. (2009). *Determination of the degree of preferred orientation within the March–Dollase approach. J. Appl. Cryst.* **42**, 513–518.

references